Pergamon

Geochimica et Cosmochimica Acta, Vol. 68, No. 3, pp. 653–672, 2004

0016-7037/04 $30.00 + .00

doi:10.1016/S0016-7037(03)00448-4

Experimental reproduction of classic barred olivine chondrules: Open-system behavior of chondrule formation

AKIRA TSUCHIYAMA,[1,*] YUICHI OSADA,[1] TSUKASA NAKANO,[2] and KENTARO UESUGI[3]

[1]Department of Earth and Space Science, Graduate School of Science, Osaka University, 1-1 Machikaneyama-cho, Toyonaka, 560-0043, Japan
[2]Geological Survey of Japan, National Institute of Advanced Industrial Science and Technology (AIST), 1-1-1 Higashi, Tsukuba, 305-8567, Japan
[3]Japan Synchrotron Radiation Research Institute (JASRI/SPring-8), 1-1-1 Kouto, Mikazuki, 679-5198, Japan

(*Received January* 21, 2003; *accepted in revised form June* 23, 2003)

Abstract—Barred olivine (BO) chondrule texture with olivine rim was successfully reproduced by cooling experiments under evacuated conditions for an FeO-rich, alkali-free, low liquidus (1215°C), analog chondrule composition. The rim formation requires a heating temperature about 100°C or more above the liquidus to promote heterogeneous nucleation of olivine on the surface of a melt droplet. Partial evaporation (mainly FeO) enhances the selective nucleation too because the surface should be cooler than the interior due to the latent heat of the evaporation. The evaporation also causes subsequent growth along the cooler surface. This rim formation process suggests chondrule formation as open systems. If evaporation occurred during chondrule formation, evaporation of Na and SiO_2 should enhance the selective nucleation and growth to form olivine rims more easily. Textures close to classic BO, which consists of a single set of parallel olivine platelets with olivine rim, were also reproduced by using small samples ($<$10 mg and $<$1 mm in diameter), where only a limited number of nucleation events is possible in a small surface area. Three-dimensional structures of reproduced BO chondrules were observed by X-ray microtomography using synchrotron radiation. Olivine bars in a two-dimensional section are really platelets and the platelets grow from the surface of a melt spherule inwards. The crystallographic orientations of the olivine platelets, which are normal to the b-axis, are also consistent with those of natural BO chondrules. BO textures close to natural chondrules were formed by heating at super-liquidus temperatures of about 100–200°C for 10 min and cooled at 1000°C/h. However, detailed morphologies of olivine rims and platelets (glass inclusions and dendritic side arms) and olivine zoning are inconsistent with those of natural olivine irrespective of the experimental conditions. These discrepancies can be explained by annealing. Diffusion calculations for cooling and annealing of chondrules suggest that annealing at low temperatures ($<\sim$1000°C), such as by thermal metamorphism, cannot explain Mg-Fe and Ca zoning in BO. The annealing was possibly due to multiple heating in connection with chondrule recycling process.

1. INTRODUCTION

Chondrules are submillimeter spherical objects mainly composed of silicates and characteristically included in chondrites. It is widely accepted from their textural and chemical features that they were formed by heating of solid precursors and subsequent rapid cooling from either fully or partially molten states in the primordial solar nebula (e.g., Grossman et al., 1988). The major internal textures of chondrules are divided into two broad categories: porphyritic and nonporphyritic. Nonporphyritic textures include barred olivine, radial pyroxene and cryptocrystalline. Porphyritic chondrules, which account for more than 80% of chondrules (Grossman et al., 1988), were formed from partially molten states while nonporphyritic chondrules from fully molten states (e.g., Tsuchiyama and Nagahara, 1981; Hewins, 1988; Lofgren, 1996).

Barred olivine (BO) chondrules account for $\sim$5% of chondrules (Grossman et al., 1988). They are characterized by parallel set(s) of olivine bars in a thin section. It had been considered that olivine bar crystals are actually platy. Lately this was confirmed by X-ray computed tomography (CT) (Tsuchiyama et al., 2000) and sequential grinding (Noguchi et al., 2002). These platy olivine crystals are embedded in a glass or mesostasis and the crystallographic orientations of olivine crystals in a parallel platelet domain are identical. A BO chondrule usually has an olivine crystal that covers the chondrule surface. This olivine rim has the same crystallographic orientation as inner olivine platelets, which connect to the rim (this rim is different from so-called accretionary rim or igneous rim composed of fine- or coarse-grained material surrounding chondrules). A chondrule with a single set of parallel olivine platelets with an olivine rim is described as a "classic" BO chondrule while one with multiple sets of parallel olivine platelets as a "multiple" BO chondrule (Weisberg, 1987). BO chondrules are regarded as rapid crystallization products, where olivine crystals grow with morphologic instability, like dendritic growth. Such rapid growth occurred due to nucleation delay of olivine from supercooled melts (Tsuchiyama et al., 1980; Hewins, 1988; Lofgren and Lanier, 1990).

Experiments reproducing BO chondrules have been carried out to elucidate conditions for their formation. BO or similar textures were produced in a laboratory by Nelson et al. (1972), Donaldson (1976) and Blander et al. (1976). Tsuchiyama et al. (1980) and Tsuchiyama and Nagahara(1981) succeeded in producing BO chondrules in controlled cooling experiments from super liquidus temperatures and estimated cooling rates for BO chondrules. Since then, many experiments were made to repro-

* Author to whom correspondence should be addressed (akira@ess.sci.osaka-u.ac.jp).

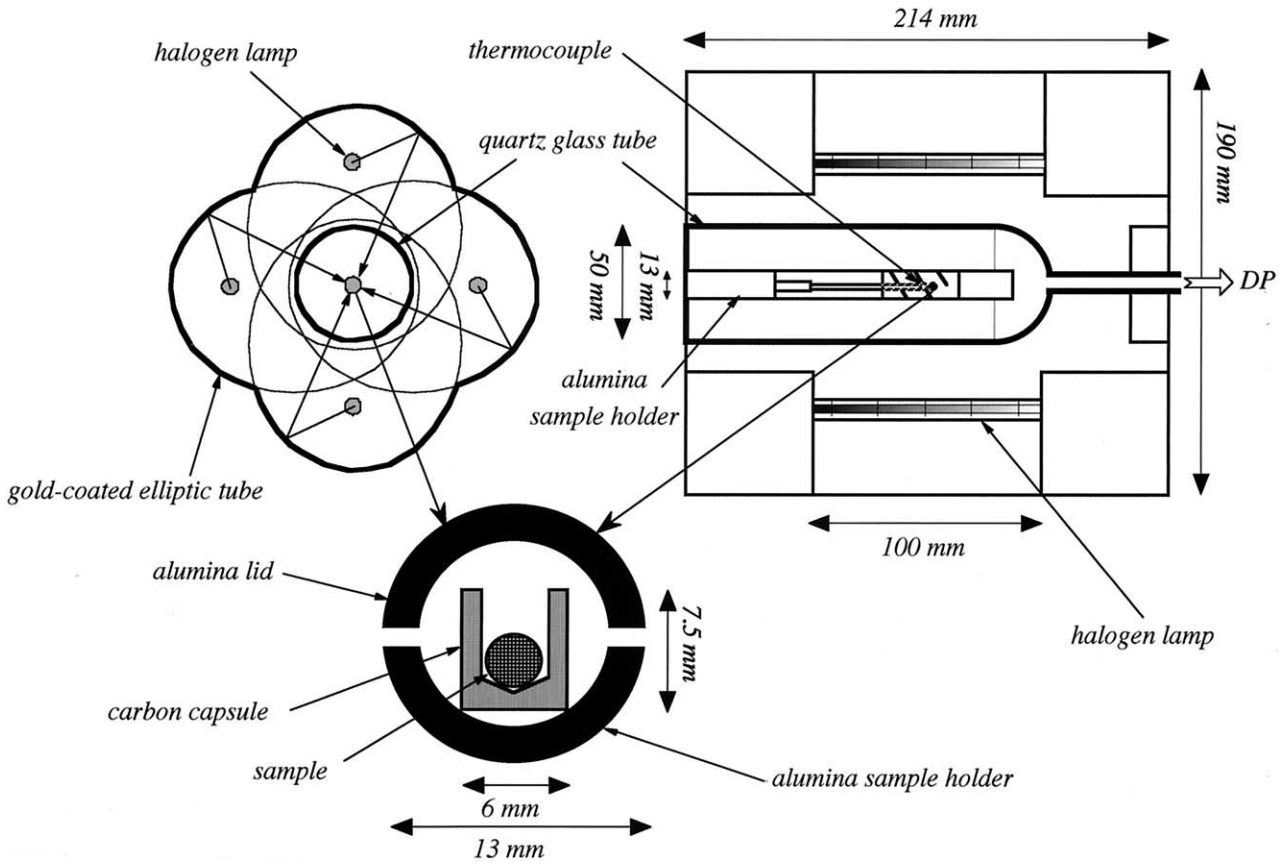

Fig. 1. Schematic illustrations of the gold image furnace and a sample.

duce BO textures (Lofgren and Russell, 1985; Lofgren, 1987, 1989; Radomsky and Hewins, 1987, 1990; Connolly et al., 1988; Radomsky, 1988; Lofgren and Lanier, 1990; Connolly and Hewins, 1991). Lofgren and Lanier (1990) carried out systematic experiments and obtain cooling rates of 500 to 2300°C/h. Connolly and Hewins (1995) produced BO textures by seeding of olivine crystals to super-cooled melts. Connolly et al. (1998) made "flash melting" experiments, where FeO-rich melts were heated at super-liquidus temperatures of a few hundreds to 400°C for short periods (a few s.), rapidly cooled to the liquidus temperatures (2800°C/h) and cooled at different rates. In these experiments, BO textures were reproduced at cooling rate of 500°C/h. From the previous experiments, the ranges of the maximum heating temperatures and heating periods were estimated as well as cooling rates. However, in the previous experiments made at one atmosphere, olivine rims have not been produced except for a limited number of runs (fig. 5b of Lofgren and Lanier, 1990; fig. 4 of Radomsky and Hewins, 1990; fig. 2b of Connolly et al., 1988). Moreover, single BO textures have not been produced except for a seeded experiment (Radomsky and Hewins, 1990). Although Connolly et al. (1988) reported an almost classic BO texture, no systematic experiments have been done to reproduce classic BO texture. Tsukamoto et al. (1999, 2001) produced rim structure in very rapid cooling experiments with a forsterite melt levitated aeroacoustically.

The main purposes of the present study are to reproduce BO rim and finally classic BO chondrule. In the present study, the following working hypotheses were made for rim formation: (1) Chondrules formed as open systems (e.g., Huang et al., 1996; Sears et al., 1996; Cohen et al., 2000), where relatively volatile elements (e.g., Na, K, Fe and probably Si) were partially evaporated from chondrule melts during chondrule formation. (2) These elements were depleted near the surfaces of the melts by the evaporation from the surfaces. (3) The depletion caused increase of olivine liquidus temperatures and thus increases of the degrees of supersaturation near the surface. (4) Olivine nucleated selectively at the more supersaturated surfaces, grew along the surfaces and thus rim structures formed. To verify these hypotheses, we made cooling experiments together with evaporation in vacuum.

It has been pointed out that the number of parallel olivine platelet domains corresponds to the number of olivines nucleated in a BO chondrule during cooling (Lofgren and Lanier, 1990). We tried to suppress the number of nucleation sites by decreasing the volume of melts to reproduce classical BO textures. The crystallographic orientations and chemical compositions of olivine were examined to compare with natural BO. The crystallographic orientation of experimental BO has not been determined yet as far as the authors know. Three-dimensional structures of reproduced BO textures were also examined for the first time by X-ray computed tomography (X-ray CT) using synchrotron radiation (Uesugi et al., 1999) to discuss growth of olivine platelets. From these results, we

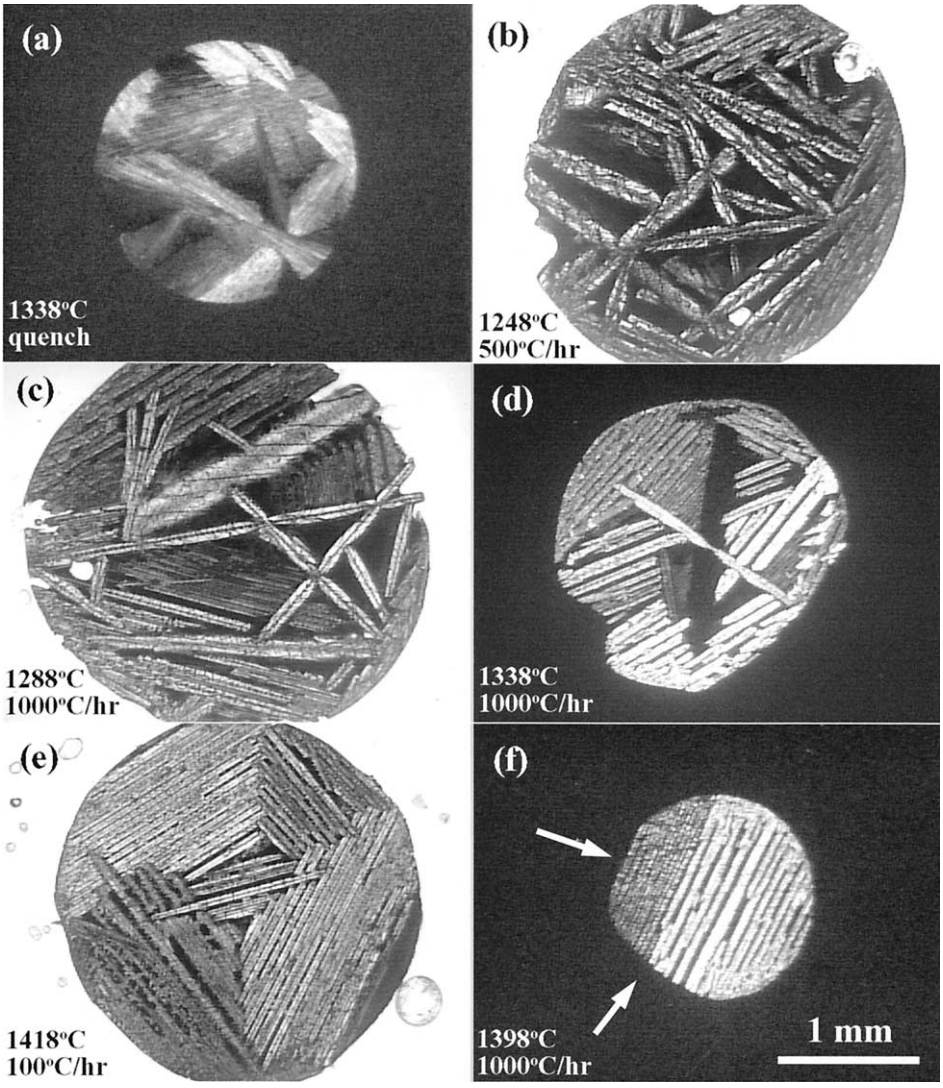

Fig. 2. Photomicrographs of run products (thin sections) showing variety of textures. (a) Run 26 (spherulitic texture with type c rim) heated at 1338°C for 10 min and cooled by shutting off the electrical power supply (crossed polarized light). (b) Run 36 (type 3 texture with type b rim) heated at 1248°C for 10 min and cooled at 500°C/h (plain polarized light). (c) Run 10 (type 2 texture with type b rim) heated at 1288°C for 10 min and cooled at 1000°C/h (plain polarized light). (d) Run 22 (type 2 texture with type a rim) heated at 1388°C for 10 min and cooled at 1000°C/h (cross polarized light). (e) Run 19 (type 1 texture with type a rim) heated at 1418°C for 10 min and cooled at 1000°C/h (plain polarized light). (f) Run 40 (type 1+ texture with type a rim) heated at 1398°C for 10 min and cooled at 1000°C/h (cross polarized light). Arrows show the surface that was in contact with a graphite capsule. Scale bar = 1 mm for all.

discussed BO formation processes and made further constraints on the BO chondrule formation.

2. EXPERIMENTAL PROCEDURES

A very FeO-rich, low liquidus (1215°C), analog chondrule composition, which is similar to that of Connolly et al. (1998), was used as a starting material in the present experiments because (1) it was easily melted by the present furnace (the maximum working temperature of the furnace is ~1500°C) and (2) large amounts of evaporation (such as FeO) was expected. Moreover, information of olivine growth was expected from Mg-Fe zoning with large compositional variations. The starting material was prepared from reagent-grade oxides except for CaO and MnO. ($CaCO_3$ and $MnCO_3$ were used, respectively). FeO was prepared from $FeC_2O_4 \cdot 2H_2O$ by heating in an H_2/CO_2 gas stream. The mixture of these materials was ground in an agate mortar for 50 min, put in an alumina Tanman tube and heated in a 1 atm H_2/CO_2 gas-mixing furnace at 1000°C and oxygen fugacity of 1.0 log unit above the iron-wustite (IW) buffer curve for 1 h. The chemical composition of the starting material was determined from an experimental charge heated at a temperature above the liquidus (1238°C) for 2 min and cooled rapidly (~20,000–30,000°C/h). The chemical compositions of glass and very fine quenched crystals in this charge were measured by an electron probe micro analyzer (EPMA) and the mean value of 20 points was adopted (Table 1). Na_2O and K_2O

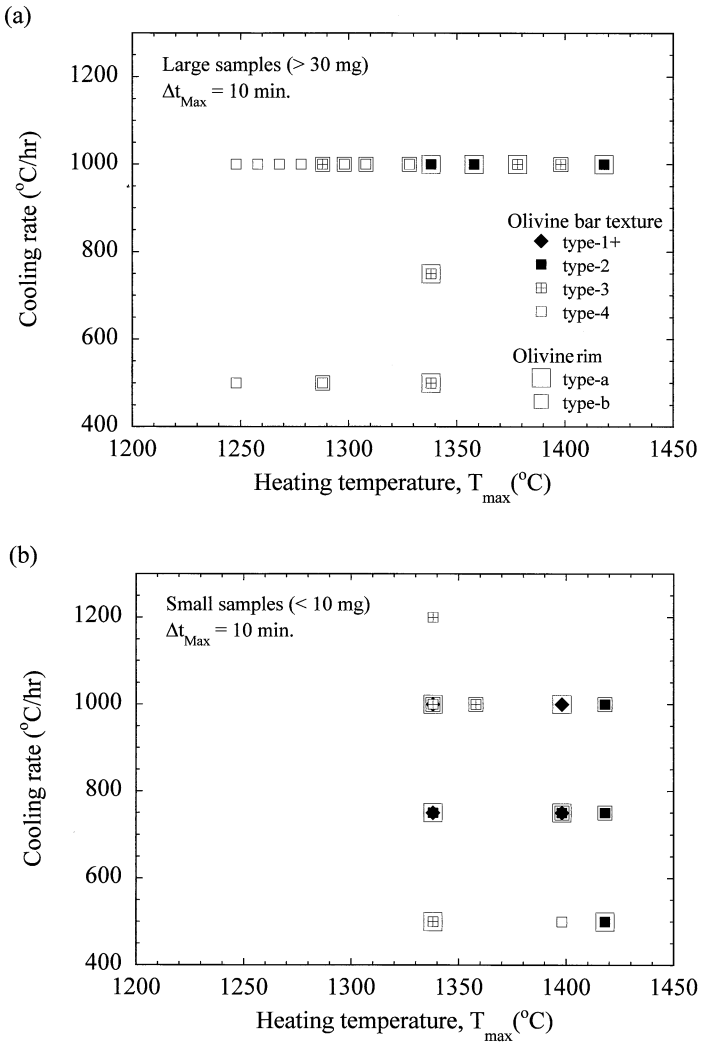

Fig. 3. Textures of run products plotted in a cooling rate – heating temperature (T_{max}) diagram (heating duration: Δt_{max} = 10 min). (a) Large samples (>30 mg). (b) Small samples (<10 mg). Rim types a and b are shown by large and moderate squares, respectively, enclosing the symbols for olivine bar texture types.

were not included in the present starting material to avoid reaction of evaporated alkalis with a quartz tube of the furnace.

Experiments were performed in an infrared gold image furnace (RHL-E44VHT, ULVAC Riko, Inc.). The furnace has four elliptic tubes (Fig. 1). A linear halogen lamp is located in one of the focus line of each tube. The other focus lines are located commonly at the center of the furnace. The surfaces of the tubes are plated by gold to reflect light as much as possible. 2 to 45 mg of starting material powder was put into a graphite or amorphous carbon capsule (4 and 6 mm in inner and outer diameters, respectively, 7.5 mm in height and ~5 mm in depth) (Fig. 1). The capsule was located in the central part of the common focus line and heated by irradiation of light from the four halogen lamps. The capsule was held by a half pipe of alumina (13 mm in diameter), which was set in a quartz glass tube (50 mm in diameter and ~150 mm in length). Another short half pipe of alumina (13 mm in diameter and 38 mm in length) was placed on the alumina sample holder and covered the capsule to homogenize the capsule temperature and to prevent direct effusion of elements (mainly Fe) from the sample to the quartz tube. The volume inside the quartz tube was evacuated by a diffusion pump (DP). The pressure was measured by an ion gauge set at the left end of the quartz tube in Figure 1. The pressure was $\sim 1.3 \times 10^{-3}$ Pa. Sample temperatures were measured and controlled by a Pt-PtRh13 thermocouple located closed to the capsule. The thermocouple was calibrated against the melting point of gold. The capsule was heated rapidly to 200°C and at the rate of 230°C/h to the maximum temperature, T_{max}, ranging from 1238 to 1418°C. After holding at T_{max} for 0 to 120 min it was cooled at 500 to 1200°C/h to 800°C and quenched. Some of them were quenched directly from T_{max}. The quenching was made by shutting off the power supply to the halogen lamps. In this case, the cooling rate varied from ~40,000°C/h at T_{max} to ~7000°C/h at 800°C. The experimental conditions are summarized in Table 2.

Oxygen fugacity in the furnace was affected by residual air during evacuation (Tsuchiyama and Fujimoto, 1995). If 20% of the gas in the furnace was oxygen, the oxygen fugacity should

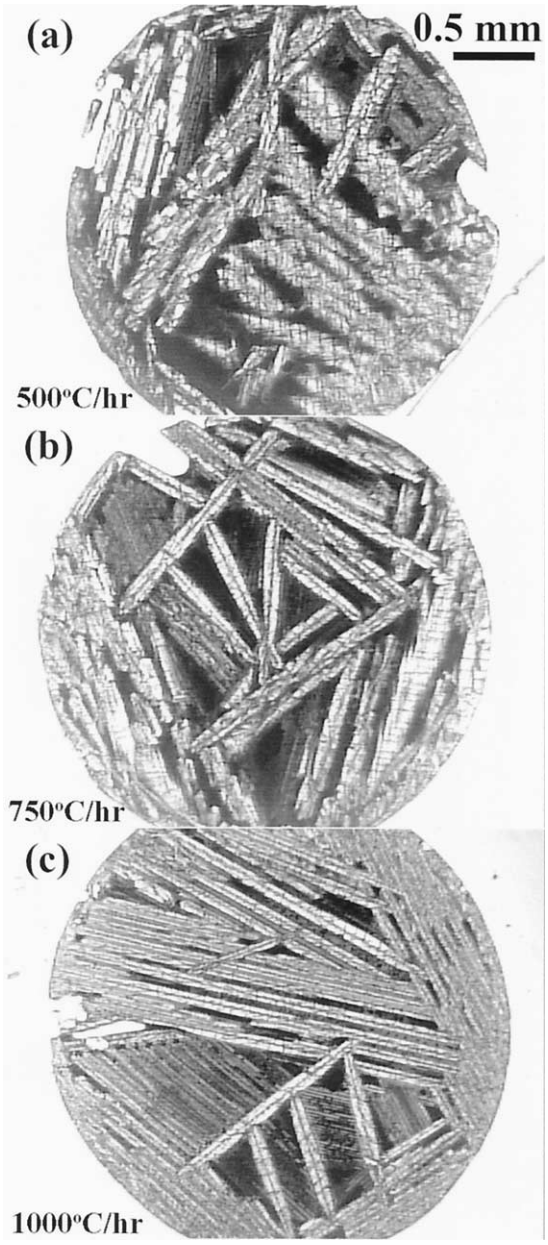

Fig. 4. Photomicrographs of run products (thin sections: plain polarized light) showing change in olivine plate morphology by cooling rate (heated at 1338°C for 10 min). (a) Run 20 (type 2 texture with type a rim) cooled at 500°C/h. (b) Run 21 (type 2 texture with type a rim) cooled at 750°C/h. (c) Run 15 (type 1 texture with type a rim) cooled at 1000°C/h. The scale bar of 0.5 mm is common to all.

be $\sim 3\times10^{-4}$ Pa. This oxygen fugacity at 1200 to 1420°C is higher than that of the fayalite-magnetite-quartz buffer curve. On the other hand, graphite (or amorphous carbon) acts as a reducing agent. Any magnetite and metallic iron were not observed in all the experimental charges and the capsules. Probably, the effects of the residual air and carbon were canceled and ferrous iron state was maintained in the charges during the experiments. Fe metal is more volatile than Fe silicate (Cohen, 2002). This might explain the absence of Fe metal alternatively.

As wetting between graphite (or amorphous carbon) and silicate melts is bad, the melted samples became spherical to minimize the contact area between them. We used small samples (most of them are <10 mg and <1 mm in diameter) to suppress the number of nucleation sites. However, in this case, the melt shapes deviated from spherical shapes due to some inevitable contact between melt surface and the inner bottom of the capsule (Fig. 2f; also see Figs. 6, 7a, and 13a). Therefore, graphite capsules with polished bottom surfaces or amorphous carbon capsules with smoother bottom surfaces were also used to minimize the contact in some runs. The weight of each sample before and after the run was measured to evaluate evaporation. To evaluate evaporation component(s), the chemical composition of the run product with the maximum weight loss (18.9%) (run 54) was obtained from the mean chemical compositions of olivine and glass analyzed by EPMA and their modal compositions (Table 1).

After the experimental charges were observed under a binocular microscope, they were mounted in epoxy and polished thin sections were made. They were observed under an optical microscope and a scanning electron microscope (SEM) at Osaka University (JEOL T220). The crystallographic orientations of olivine crystals were determined by an optical microscope with a universal stage (U-stage). The orientations were measured twice and the mean values were adopted. Those of BO chondrules in natural samples (Allende (CV3), Axtell (CV3), Maralinga (CK4), Julesburg (L3), Tulia (H3-4), Beaver (L5) and Fukutomi (L5)) were also measured for comparison. The chemical compositions of olivine and glass were determined with EPMA at Osaka University (JEOL 733). The analyses were made at 15 kV accelerating voltage and 12 nA beam current with a focused beam. Natural and synthetic minerals were used as standards. Correction was made with the ZAF method.

Three-dimensional structures of charges (runs 63 and 64) were obtained with an X-ray microtomography system using synchrotron radiation at BL20B2 in SPring-8, Nishiharima, Japan (SP-μCT; Uesugi et al., 1999). The photon energy was 30 keV. 360 projections were obtained for each sample. CT slice images (1000×1000 matrix) were reconstructed from the projections using the convolution back projection algorithm. Three-dimensional structures were reconstructed from successive 220 to 240 slices. The size of the voxel (imaging element in three-dimension; like pixel in two-dimension) of the CT images is $5.83 \times 5.83 \times 5.83$ μm. This gives spatial resolution of ~13 μm (Uesugi et al., 1999). Enlarged three-dimensional plaster models (6–6.5 cm in diameter: x ~50 magnification) were made from the CT images by rapid prototyping method using a 3D printer (Z406 System, Z Corporation) at Tsukuba Advanced Computing Center (TACC), AIST in Japan. This 3D printer uses a powder-binder technology to create three-dimensional models directly from digital data. The 3D printer spreads a thin layer of plaster powder, an ink-jet print head prints a binder in the cross-section of the model being created, a build piston drops down, making room for the next layer, and the process is repeated.

The liquidus temperature of the starting material was determined by melting experiments. A starting material (~30 mg) was pressed into a pellet of ~3 mm in diameter, hung with a Pt wire loop (0.2 mm in diameter), heated at different tempera-

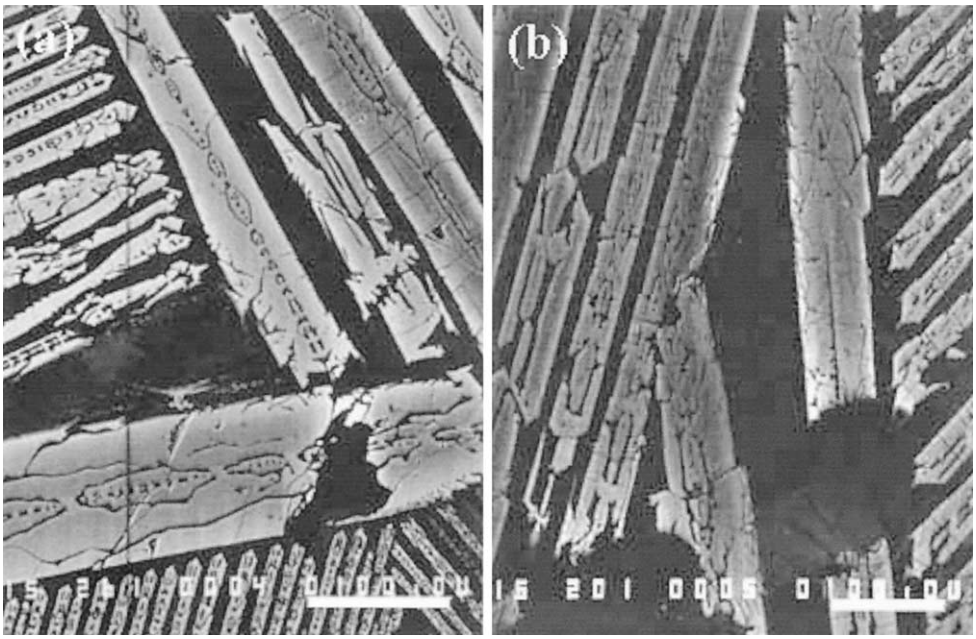

Fig. 5. BSE images of run product 15 (Fig. 4c) heated at 1338°C for 10 min and cooled at 1000°C/h. Mg-Fe zoning is seen in olivine bars. Dark matrix is glass. Scale bars are 100 μm.

tures ranging from 1200 to 1238°C for 40 to 60 min in a 1 atm gas-mixing furnace and quenched into water. The oxygen fugacity (0.5 log unit below the IW buffer curve) was controlled by a H_2/CO_2 gas mixture. The liquidus phase was olivine and the liquidus was between 1215 and 1220°C. As pure platinum was used as wires, a small amount of Fe was lost to the wires due to alloying of Fe to the wires (the thickness of an Fe-rich layer near the surface is ~20 μm with the maximum Fe content of the order of 30 wt%). This might increase the measured liquidus temperature slightly. Thus, we adopted the liquidus temperature of ~1215°C here.

Table 1. Chemical compositions of starting materials and run 54.

Element	This study (wt %)	Previous study[a] (wt %)	Run 54[b] (wt %)	Run 54[c] (wt%)
MgO	2.88	2.81	3.1	3.5
Al_2O_3	3.66	3.67	5.4	4.5
SiO_2	37.41	35.48	45.2	46.1
CaO	2.51	2.63	4.0	3.1
TiO_2	0.21	0.19	0.3	0.3
MnO	0.33	0.16	0.3	0.4
FeO	53.02	52.94	41.8	42.0
Na_2O	0.00	0.39	0.0	0.0
K_2O	0.00	0.15	0.0	0.0
Total	100.00[d]	98.42	100.0[d]	100.0[d]
Liquidus temperature	1215°C	1211°C		

[a] Connolly et al. (1998).
[b] Bulk composition of run 54 estimated from the chemical analyses of olivine and glass and their modal comosition (57.5 vol% olivine).
[c] Bulk composition of run 54 estimated by evaporation loss of FeO alone (18.9% loss).
[d] Calculated as the total of 100 wt%.

3. RESULTS

3.1. Olivine Bar Textures

All the run products were composed of olivine and glass. Textures produced in the present experiments are summarized in Table 2. BO texture was produced in a wide range of experimental conditions except for quench experiments, where spherulitic of radial olivine texture was formed (Fig. 2a). Different types of BO textures were formed by cooling at 500–1200°C/h from different maximum temperature, T_{max}. Examples are shown in Figures 2b–f (heating duration at T_{max} of 10 min). If T_{max} was slightly higher than the liquidus temperature, T_{liq} (1215°C), or the degree of superheating, $+\Delta T$ ($= T_{max} - T_{liq}$), was low, the charge was composed of many sets of olivine bars with different directions and different widths (Fig. 2b: T_{max} = 1248°C). We will call such textures with olivine bars type 3 here. If T_{max} was sufficiently higher than T_{liq} (large $+\Delta T$) for large samples (>30 mg), the number of olivine bar sets was relatively small and the widths of the bars were quite uniform (Fig. 2e: T_{max} = 1418°C). These olivine bar textures are similar to those of multiple BO chondrules and are called type 1. Intermediate olivine bar textures (type 2) formed at intermediate T_{max} or $+\Delta T$ (Fig. 2c: T_{max} = 1288°C). The number of olivine bar sets decreases with decreasing the sample size. For small samples textures between types 2 and 1 formed at intermediate $+\Delta T$ (Fig. 2d: T_{max} = 1338°C). Textures with almost a single set of parallel olivine bars (type 1+) formed at large $+\Delta T$ (Fig. 2f: T_{max} = 1398°C). The texture type − cooling rate − T_{max} relation is shown in Figure 3 for large (>30 mg) and small (<10 mg) samples, respectively.

With increasing cooling rate, the width of olivine bars becomes fine (Fig. 4). A quantitative bar width-cooling rate relation of this type was reported by Lofgren and Lanier (1990).

Table 2. Experimental conditions and results.

Run	Temperature (°C)	Duration (min)	Cooling rate (°C/h)	Initial wt. (mg)	Final wt. (mg)	Wt. loss (%)	Texture[a]	Rim[b]	S[c] (mm^2)	$\Delta m/S^c$ (mg/mm^2)	Capsule[d]	Remarks
3	1238	0	1000	45.3	44.9	0.9	3	b	25.99	0.015	G	
65	1238	2	quench	22.7	22.6	0.4	4	n	16.46	0.024	AC	For starting composition
2	1238	30	1000	40.3	39.9	1.0	3	c	24.01	0.017	G	
1	1238	30	quench[e]	30.0	29.6	1.0	4	c	19.70	0.016	G	
4	1248	0	1000	39.0	38.8	0.5	3	–	23.58	0.008	G	
6	1248	5	1000	41.1	n.d	n.d	4	c	n.d	n.d	G	
36	1248	10	500	38.6	38.2	1.1	3	c	23.31	0.019	G	
5	1248	10	1000	43.6	43.2	0.9	3	c	25.33	0.016	G	
7	1258	10	1000	43.3	42.8	1.2	3	c	25.17	0.020	G	
8	1268	10	1000	41.3	41.1	0.5	3	c	24.50	0.008	G	
9	1278	10	1000	39.5	39.3	0.5	3	c	23.78	0.008	G	
35	1288	10	500	38.6	37.9	2.0	3	b	23.20	0.033	G	
10	1288	10	1000	43.8	43.3	1.1	2	b	25.37	0.020	G	
11	1298	10	1000	41.8	41.3	1.2	3	b	24.58	0.020	G	
12	1308	10	1000	43.3	42.7	1.4	3	b	25.13	0.024	G	
13	1318	10	1000	42.7	42.3	0.9	2	–	24.98	0.016	G	
14	1328	10	1000	41.9	41.4	1.2	3	b	24.62	0.020	G	
20	1338	10	500	37.2	36.7	1.3	2	a	22.72	0.022	G	
21	1338	10	750	40.0	39.6	1.0	2	a	23.90	0.017	G	
15	1338	10	1000	43.0	42.4	1.4	1	a	25.01	0.024	G	
16	1358	10	1000	41.8	41.2	1.4	1	a	24.54	0.024	G	
17	1378	10	1000	35.3	34.8	1.4	2	a	21.93	0.023	G	
18	1398	10	1000	36.0	35.2	2.2	2	b	22.10	0.036	G	
19	1418	10	1000	36.5	35.6	2.5	1	a	22.26	0.040	G	
33	1338	10	500	8.31	8.03	3.4	2	a	8.25	0.034	G	
39	1338	10	500	4.46	4.25	4.7	1	a	5.40	0.039	G	
29	1338	10	750	4.57	4.46	2.4	1	a	5.57	0.020	G	
30	1338	10	750	4.75	4.55	4.2	1	c	5.65	0.035	G	
38	1338	10	750	7.88	7.66	2.8	3	—	7.99	0.028	G	
22	1338	10	1000	15.5	15.2	2.1	2	a	12.63	0.022	G	
27	1338	10	1000	7.31	7.17	1.9	1	a	7.65	0.018	G	
37	1338	10	1000	5.02	4.90	2.4	1+	b	5.93	0.020	G	
64	1338	10	1000	4.14	3.69	10.9	2	a	4.91	2.213	Gp	For X-ray CT (011026b)
31	1338	10	1200	6.84	6.59	3.7	2	c	7.23	0.035	G	
25	1338	10	quench	12.8	n.d	n.d	4	c	n.d	n.d	G	
26	1338	10	quench	11.8	11.4	3.1	4	c	10.42	0.038	G	
60	1338	10	1000–500	2.16	2.03	6.0	1+	a	3.30	0.039	AC	
43	1338	15	1000	4.91	4.51	8.2	2	c	5.62	0.071	Gp	
56	1338	20	750	6.81	6.55	3.8	1	b	7.20	0.036	Gp	
44	1338	20	1000	6.66	6.32	5.1	1+	b	7.03	0.048	Gp	
57	1338	30	750	5.86	5.41	7.7	1	c	6.34	0.071	Gp	
45	1338	30	1000	6.15	5.56	9.6	1	b	6.46	0.091	Gp	
58	1338	40	750	6.57	6.12	6.9	1+	c	6.88	0.065	Gp	
48	1338	40	1000	6.45	5.97	7.4	1+	a	6.77	0.071	Gp	
49	1338	50	1000	6.16	5.68	7.8	2	b	6.55	0.073	Gp	
46	1338	60	1000	7.03	6.50	7.5	2	a	7.17	0.074	Gp	
47	1338	120	1000	6.94	6.20	10.7	2	—	6.94	0.107	Gp	
24	1358	10	1000	14.3	14.0	2.0	2	a	11.96	0.023	G	
59	1358	10	1000	3.25	3.11	4.3	2	b	4.38	0.032	AC	
62	1358	20	1000	2.13	2.02	5.2	1	a	3.29	0.033	AC	
42	1398	10	500	4.27	3.96	7.3	3	c	5.15	0.060	Gp	
41	1398	10	750	4.51	4.28	5.3	1+	a	5.42	0.042	Gp	
63	1398	10	750	4.56	4.49	1.5	1	b	5.60	0.274	Gp	For X-ray CT (011026a)
61	1398	10	1000–500	2.77	2.62	5.4	1	a	3.91	0.038	AC	
40	1398	10	1000	5.83	5.63	3.4	1+	a	6.51	0.031	G	
50	1398	20	1000	6.77	6.11	9.8	1+	c	6.88	0.096	Gp	
51	1398	30	1000	6.44	5.76	10.6	2	a	6.61	0.103	Gp	
52	1398	40	1000	6.15	5.44	11.5	3	a	6.36	0.112	Gp	
53	1398	50	1000	5.77	4.97	13.9	1	—	5.99	0.134	Gp	
55	1398	50	1000	5.94	5.01	15.7	1	a	6.02	0.154	Gp	
54	1398	60	1000	6.76	5.48	18.9	1	a	6.39	0.200	Gp	
34	1418	10	500	7.66	7.23	5.6	1	a	7.69	0.056	G	
32	1418	10	750	10.4	9.92	4.6	1	b	9.50	0.051	G	
23	1418	10	1000	19.5	18.9	3.0	2	a	14.59	0.042	G	
28	1418	10	1000	5.44	5.05	7.2	1	b	6.06	0.064	G	

[a] Olivine bar texture; type 1: parallel bars (1+: almost classic BO), 2: intermediate, 3: nonparallel bars, 4: spherulitic.
[b] Olivine rim type; a: well developed, b: moderately developed, c: almost absent,—: not determined.
[c] Capsule G: graphite, Gp: graphite with a polished bottom, AC: amorphous carbon.
[d] Quench: shutting off of electric power supply (cooling rate varies from about 40,000 to 15,000°C/hr).
[e] Evaporated mass devided by the estimated surface area of a spherule.

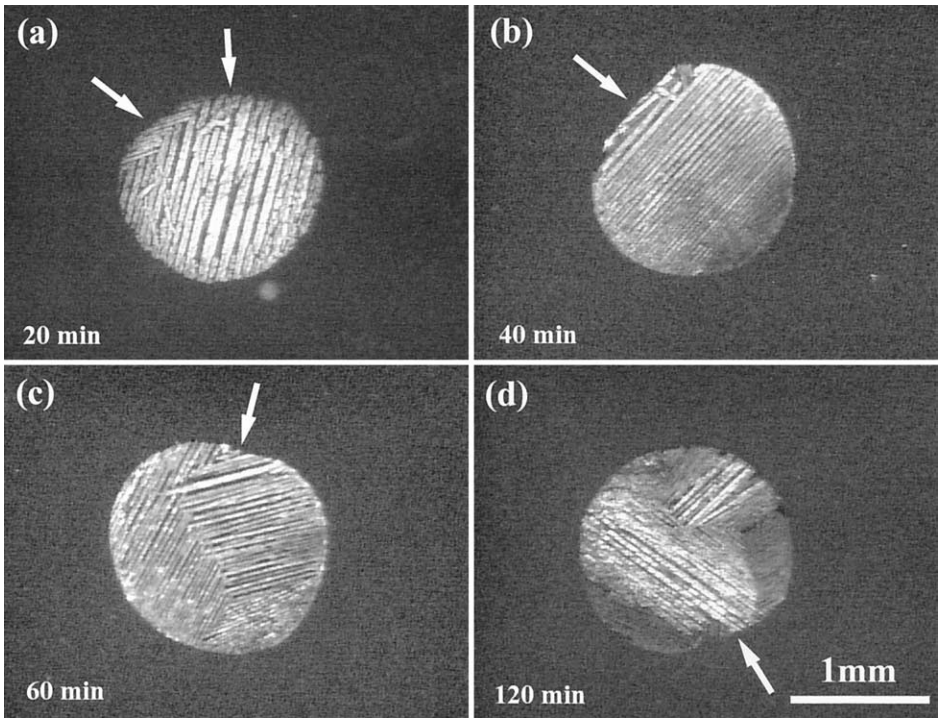

Fig. 6. Photomicrographs of run products (thin sections: cross polarized light) showing change in olivine plate morphology by heating duration (heated at 1338°C and cooled at 1000°C/h). (a) Run 44 (type 1+ texture with type b rim) heated for 20 min (b) Run 48 (type 1+ texture with type a rim) heated for 40 min. (c) Run 46 (type 2 texture with type a rim) heated for 60 min. (d) Run 47 (type 2 texture) heated for 120 min. Arrows show the surfaces that were in contact with carbon capsules. The scale bar of 1 mm is common to all.

At 500°C/h each olivine crystal is dendritic and regarded roughly as a bar (Fig. 4a). Typical bar-shaped crystals formed at higher cooling rates (Fig. 4c). In these bars, glass inclusions are always present and align more or less regularly (Fig. 5). These inclusions have variety of shapes, such as U-, X- and H-shapes, and the bar crystals are regarded as hopper-shaped or dendritic crystals with platy shapes as a whole. These features were always observed in the run products even in the classic BO type (type 1+) textures. Change in BO textures with heating duration is shown in Figure 6. With increasing heating duration at a constant T_{max} (1338°C) and cooling rate (1000°C/h), the bar width becomes fine.

3.2. Olivine Rim

Many charges have olivine rims. Observations of sample surfaces under a binocular microscope and their thin sections under a polarized microscope show that the rims are thin (<30 μm) and do not cover the whole sample surfaces (Fig. 7a). Rims are not present on the surfaces that are in contact with carbon capsules. Rims were observed usually at one end of a set of parallel olivine bars while sometimes at both ends. Morphologically, most of the rims are dendritic (Fig. 7b). Sometimes, thin crust is present along the surface (Fig. 7c). Olivine bars are connected to the rim. Olivine rim and bars share the same crystallographic orientation.

The degree of development of olivine rims was divided into three categories: (type a) olivine rim covers almost all the surface except for that in contact with the carbon capsule (Fig. 7a), (type b) olivine rim partially covers the surface and (type c) olivine rim is almost absent (Fig. 7d). In the case of type c, small olivine crystals are usually present on a limited area of the surface as an imperfect rim. Surfaces without rims are usually irregular (Fig. 7d) probably due to crystallization of platy olivine to the surface (a similar feature is seen in fig. 4E of Connolly and Hewins, 1998). Types a and b rims were developed for runs with high T_{max} (1290–1420°C for large samples and 1340–1420°C for small samples) (Fig. 3). Textures close to classic BO (type 1+ texture with type a rim) were formed for small samples (e.g., Fig. 2f) although perfect classic BO was not formed due to the contact with the carbon capsule.

3.3. Evaporation of Melt

The weight of a charge decreased after a run due to evaporation with a loss of 0.4 to 18.9 wt% (Table 2). The bulk chemical composition of the charge with the maximum weight loss (18.9%: run54) is shown in Table 1. The chemical composition for this charge was also estimated from the starting composition by assuming that the FeO component evaporated alone. The measured and estimated compositions are similar suggesting that the evaporated component was mainly FeO in the present experiments. The slight difference of the SiO_2 concentrations might be due to a small amount of SiO_2 evaporation. Any compositional gradients were not detected within the glass even near the spherule surfaces except for gradients close to olivine crystals due to overgrowth during quenching.

Figure 8 shows olivine rim types in the degree of evapora-

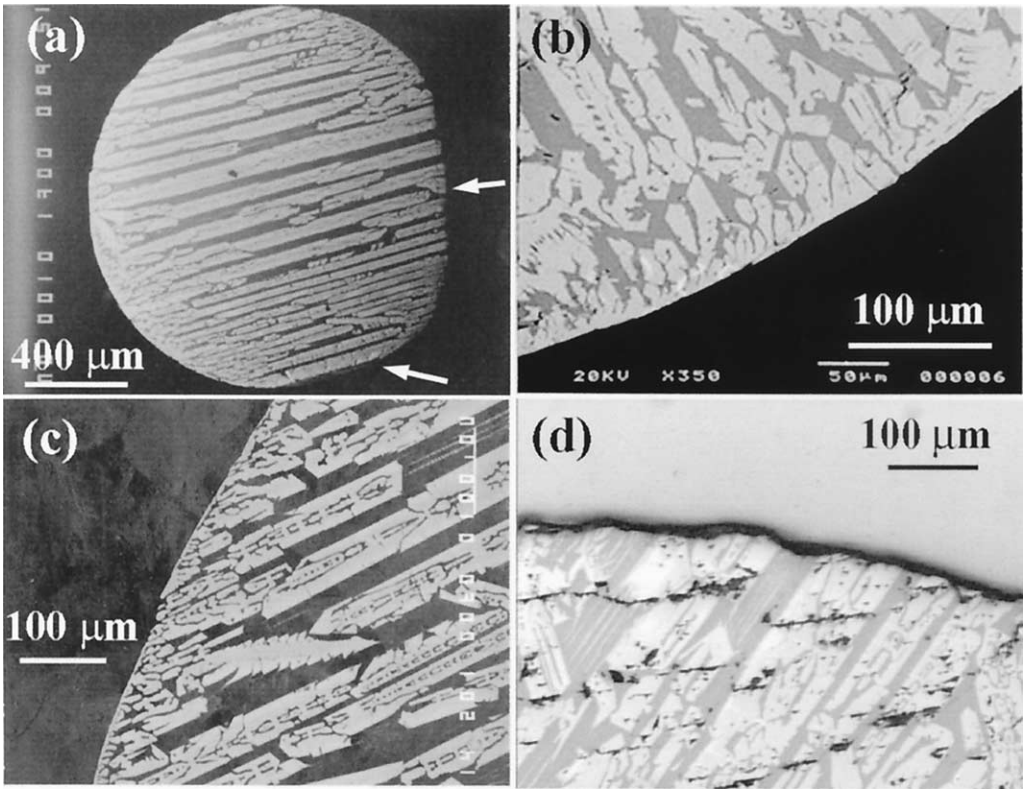

Fig. 7. Photomicrographs of run products showing olivine rim. (a) Run 40 (Fig. 2f): type 1+ texture with type a rim) heated at 1398°C for 10 min and cooled at 1000°C/h (BSE image). Arrows show the surface that was in contact with a graphite capsule. (b) Close up of a rim part of (a) (BSE image). (c) Run 16 (type 1 texture with type a rim) heated at 1358°C for 10 min and cooled at 1000°C/h (BSE image). (d) Run 30 (type 1 texture with type c rim) heated at 1338°C for 10 min and cooled at 750°C/h (reflected light).

tion, $(\Delta m/m) - T_{max}$ diagram for runs cooled at 500–1200°C/h. For large samples (>30 mg) rims develop in charges with high peak temperatures (~100–200°C above the liquidus) and large evaporation degrees ($\Delta m/m > \sim 1\%$) (Fig. 8a). For small samples (<10 mg) the rim formation does not relate to $\Delta m/m$ and some charges with large $\Delta m/m$ have type c rim (Fig. 8b).

Evaporation rates were evaluated by the evaporation mass loss, Δm, divided by the sample surface area, S, which was estimated from the sample mass by assuming the melt density of 3.6 g/cm^3. $\Delta m/S$ is plotted against T_{max} for runs with constant heating duration, Δt_{max} (10 min), and cooling rate (1000°C/h) (Fig. 9a), Δt_{max} for runs with constant T_{max} (1338°C) and cooling rate (1000°C/h) (Fig. 9b), and cooling rate for runs with constant T_{max} (1338°C) and Δt_{max} (10 min) (Fig. 9c). $\Delta m/S$ increases with increasing T_{max} and Δt_{max} while it is almost constant with increasing cooling rate. These results suggest that the evaporation occurred mainly in the peak temperature at T_{max}.

3.4. Olivine Zoning

Typical Mg-Fe zoning of olivine is shown as backscattered electron (BSE) images (Fig. 5). The marginal portion of an olivine bar is more Fe-rich than the core. Overgrowth during quenching is minor (the width of the overgrowth is 1 to a few microns as deduced from BSE images). Figure 10a shows a typical example of variation of the Mg-Fe composition along an olivine bar. The width of the olivine bar is not uniform but the width decreases from the central part to the both tips. The compositions at the tips are intermediate between the core and marginal compositions. This bar shape and its zonal structure in the two-dimensional section suggest that the olivine crystal grew as a short and thin bar with relatively Mg-rich composition ($Fa_{\sim 16}$) first, became long but still thin (growth of $Fa_{\sim 12}$), and finally overgrowth of Fe-rich marginal part ($Fa_{\sim 8}$) occurred. The CaO content is also zoned and has the negative correlation with the Mg/(Mg + Fe) ratio (Fig. 10b).

The cores of olivine bars, which were in contact with a carbon capsule, are usually most Mg-rich. This suggests that nucleation occurred at the contact surface. Unfortunately olivine rims were so small that their chemical compositions were not measured. Heterogeneity of the glass composition due to selective FeO evaporation was not observed. Sometimes, sets of parallel olivine bars with different widths are coexisting in a single charge. In this case, the core compositions of coarser bars are always more Mg-rich than those of finer bars (Fig. 5). Similar results have already been reported by Lofgren and Lanier (1990) and explained by a second generation of finer bars.

3.5. Three-Dimensional Structure

Figures 11 and 12 show a series of CT images for runs 63 and 64, respectively. Numerical expression of the shading

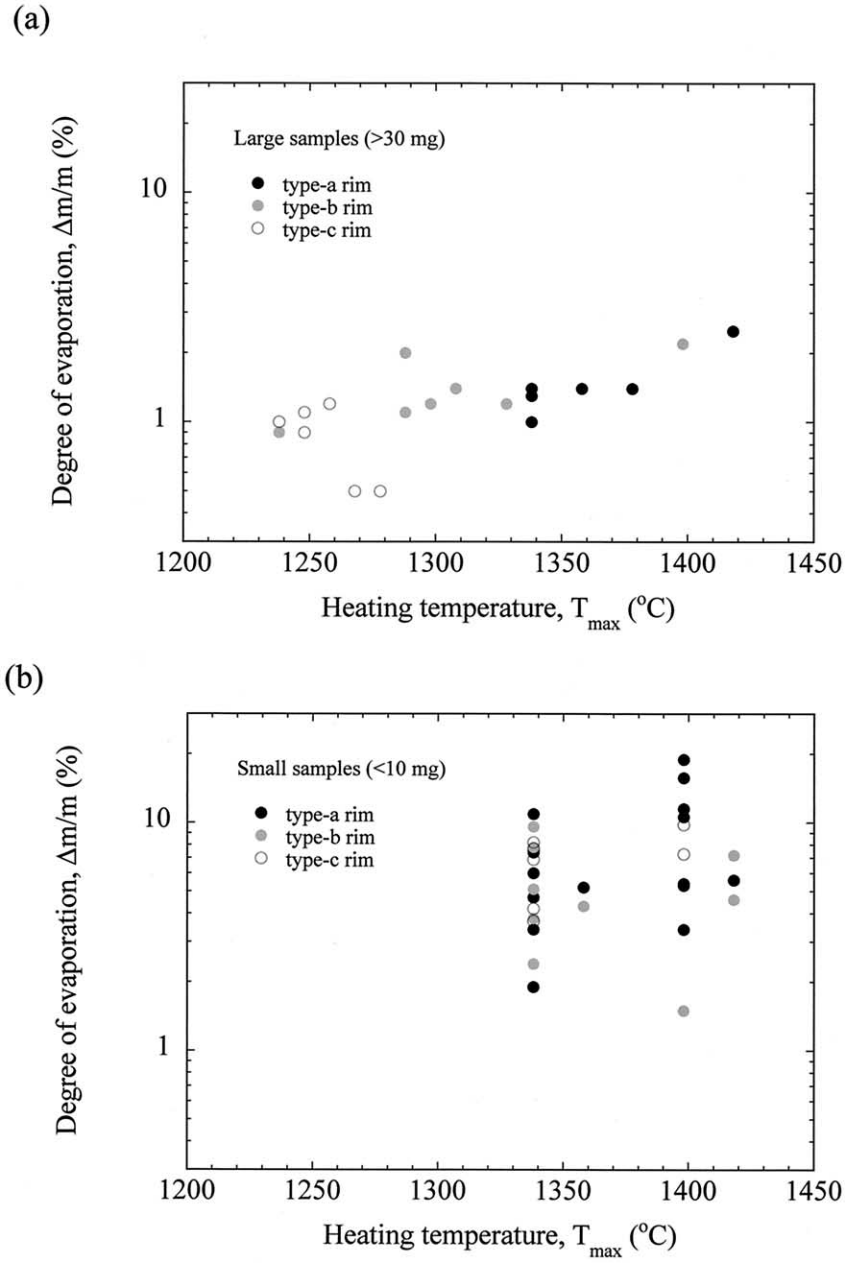

Fig. 8. Types of olivine rim plotted in a degree of evaporation (Δm/m) – heating temperature (T_{max}) diagram for runs with the cooling rate of 500–1200°C/h. (a) Large samples (>30 mg). (b) Small samples (<10 mg).

intensity in CT images is called CT value, which is calculated by the reconstruction. As we used a monochromatic beam, the CT value in the present CT images almost equals to the X-ray linear attenuation coefficient (cm^{-1} in unit), which is a function of the chemical composition and density of a material and the X-ray energy (e.g., McCullough, 1975). Accordingly, bright objects have large CT values and thus large linear attenuation coefficients and vise versa. The gray scales in Figures 11 and 12 show the relation between the CT value and the shading intensity. Olivine is recognized as white objects in gray glass. Figure 13 shows their external three-dimensional shapes, which correspond to the enlarged three-dimensional plaster models. From the three-dimensional structures, we reconfirmed that olivine crystals, which are seen as bars in two-dimensional slices, are really plates. The shapes of the olivine plates are more or less dendritic and their surfaces are not flat. Most of the plates are in contact with the spherule surfaces with or without olivine rim. Observation of the plaster model of run 63 (Fig. 13a) shows that many olivine plates, which are seen in the lower half part of the spherule in Figure 11 (set 2), are present throughout the surface. Fine plates, which can be regarded as the second-generation crystals, are bounded by sets of coarse plates and included in the spherule interior (Fig. 12).

A thin rim is partially developed on the charge of run 63

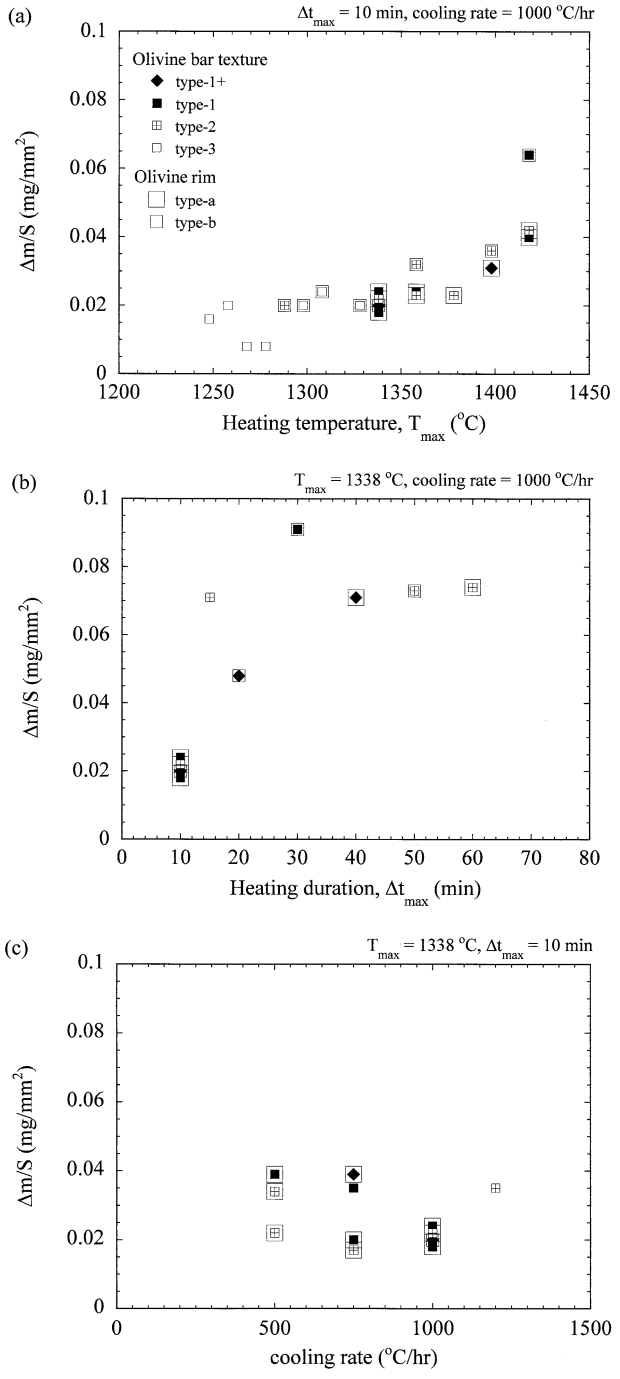

Fig. 9. Evaporation loss per unit area (Δm/S) plotted against (a) heating temperature (T_{max}) for constant heating duration (Δt_{max} = 10 min) and constant cooling rate (1000°C/h), (b) heating duration (Δt_{max}) at constant heating temperature (T_{max} = 1338°C) and constant cooling rate (1000°C/h), and (c) cooling rate with constant heating temperature (T_{max} = 1338°C) and constant heating duration (Δt_{max} = 10 min). Symbols are the same as those in Figure 3.

(e.g., surface on the left of Fig. 11h) while coarse rims are developed on the charge of run 64 (Figs. 12 and 13). Observation of the plaster model of run 64 (Fig. 13b) shows that the rims are divided into five portions, which correspond to parallel sets of olivine plates with different directions.

Two sets of olivine plates, which grew almost simultaneously, are recognized in Figure 11 (sets 1 and 2). The growth of set 1 slightly preceded set 2 because some plates of set 1 intrude into those of set 2. This feature can be explained as follows: the set 1 plates grew from the spherule surface on the top in Figure 11 and were interrupted by the set 2 plates, while the set 2 plates grew from an other part of the spherule surface inward and were interrupted by the growth front of the set 1 plates. Especially, the coarse plate, indicated by an arrow in set 1, seems to nucleate on the surface which is in contact with the graphite capsule and grow inward. Similar feature for the two sets of olivine plates is also seen in Figure 12 (set 3 plates intrude partially into set 4 plates).

3.6. Crystallographic Orientation of Olivine

The directions normal to olivine plates were plotted in a stereogram, where the b-axis of olivine was taken as the north pole and the a- and c-axes as N and E directions in the equatorial plane, respectively (Fig. 14). Most of the olivine plates in the experimental charges are normal to the b-axis within 5°. These results are consistent with natural samples. Some natural olivine plates, which have a relatively large deviation from the b-axis (up to ~20°), have wavy extinction under cross-polarized light. This suggests that the deviation was caused by shock deformation as a secondary process in the meteorite parent body. The normal directions of the olivine plates in the experimental charges seem to be concentrated towards the c-axis. This may be due to an error of the measurements although the reason is unknown.

4. DISCUSSION

4.1. Olivine Rim Formation

Olivine rims were developed in charges with high peak temperatures, T_{max}, and large evaporation degrees, Δm/m, for the large samples (Fig. 8a). In the low heating temperature runs, many olivine nuclei (or embryos) survive, and therefore there is little tendency for nucleation on the surface. In contrast, in the high heating temperature runs, fewer embryos survives and this makes internal nucleation more difficult and heterogeneous nucleation on the surface easier because of the advantage of the interfacial energy on the surface for nucleation. Rim formation requires olivine growth along the surface after the nucleation. As FeO is the main evaporated component in the present experiments, the olivine liquidus temperature should not be changed largely by the evaporation loss if we consider the phase diagram in the system FeO-MgO-SiO_2 (Bowen and Schairer, 1935). Evaporation loss of SiO_2 enhances olivine saturation at the surface but the effect should be small in the present experiments. On the other hand, the surface should become cooler than the interior by the latent heat of the evaporation. If this is the case, olivine should grow along the cooler surface in preference to penetrating into the interior and olivine rims form. The rim formation caused by evaporation is consistent with the fact that rims do not from on the surface in contact with the carbon capsule, which interrupts evaporation from the surface. In this model, what is important for the rim formation is not the total amount of the evaporation loss but evaporation during cooling, when nucleation and growth can occur. If

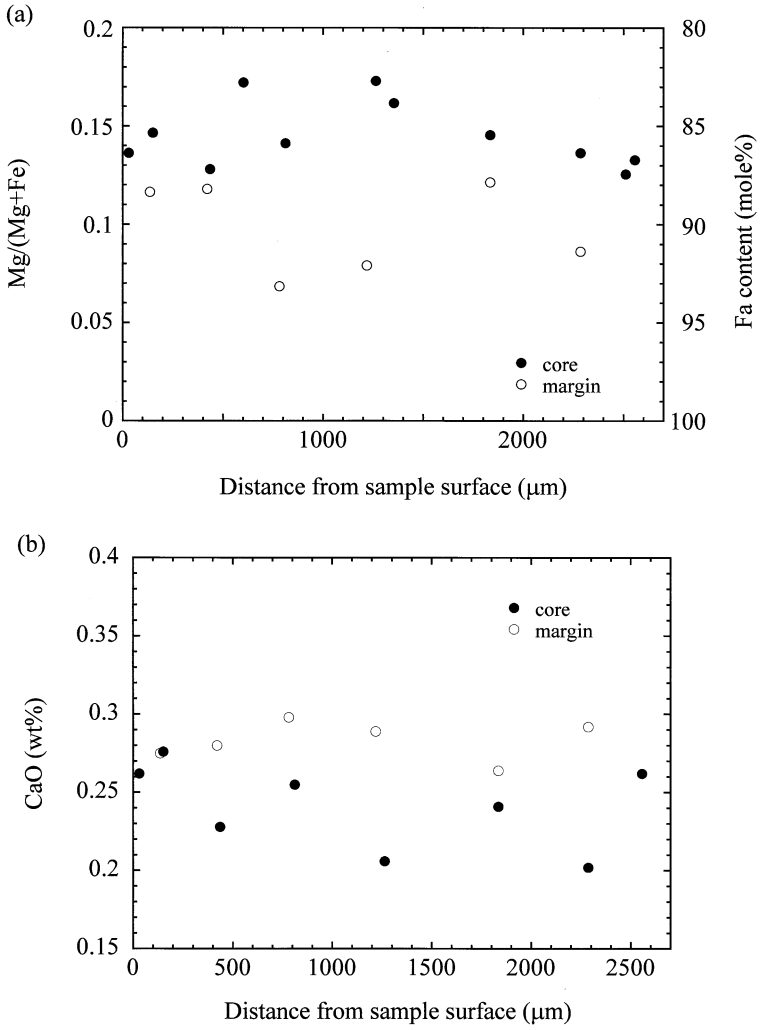

Fig. 10. A plot of olivine composition (Fa content) versus distance from sample surface. Core and marginal compositions of an olivine bar in run 15 (Fig. 4c: heated at 1338°C for 10 min and cooled at 1000°C/h) are shown as solid and open symbols, respectively. This bar has a shape like a thin lens. The maximum width at the central part of the bar is 75 μm.

heating duration at the peak temperature, t_{max}, is long, a large amount of FeO should be lost at the peak temperature and only a small amount of evaporation should occur during cooling from a refractory melt. In fact, there is a tendency that the rim development is poorer for runs with long t_{max} (Table 2 and Fig. 9b).

Rims do not always develop in the small samples even for large degrees of evaporation (Fig. 8b). This can be explained by an effect of the carbon capsules. The proportions of the surface areas in contact with the carbon capsules for the small samples are much larger than those for the large samples. An olivine rim does not develop if nucleation occurs on the contact surface without evaporation, while a rim develops if nucleation occurs on the normal surface with evaporation.

Tsukamoto et al. (1999, 2001) produced a rim structure in rapid cooling experiments with forsterite melt droplets levitated aeroacoustically. They proposed that recalescence of the melt caused the rim formation by considering release of latent heat of crystallization and growth controlled by heat transfer. Once forsterite nucleates on the surface and starts to grow, generated heat is transferred inward by thermal diffusion as well as outward by radiation. Inward olivine growth is inhibited at this stage by temperature increase in the interior of the melt spheres and thus an olivine rim should form. However, large recalescence occurring in the forsterite melt may not be expected for multi-component melts, such as chondrule melts. Moreover, the cooling rate in their experiments (~100°C/s) is much faster than that for chondrule crystallization (~1000°C/h). Therefore, this interesting idea for rim formation cannot be applied to chondrules.

Although olivine rims were formed in the present experiments, the features of these rims are not exactly the same as those of natural BO chondrules. The width of the experimental rim (<30 μm and typically 10 μm) is generally less than the natural rim (typically 20 μm or more). The morphology of the olivine rim is also different: the experimental rims are highly dendritic or skeletal and the thickness is not uniform (Figs. 7b,c), while the natural rims generally are not so dendritic or

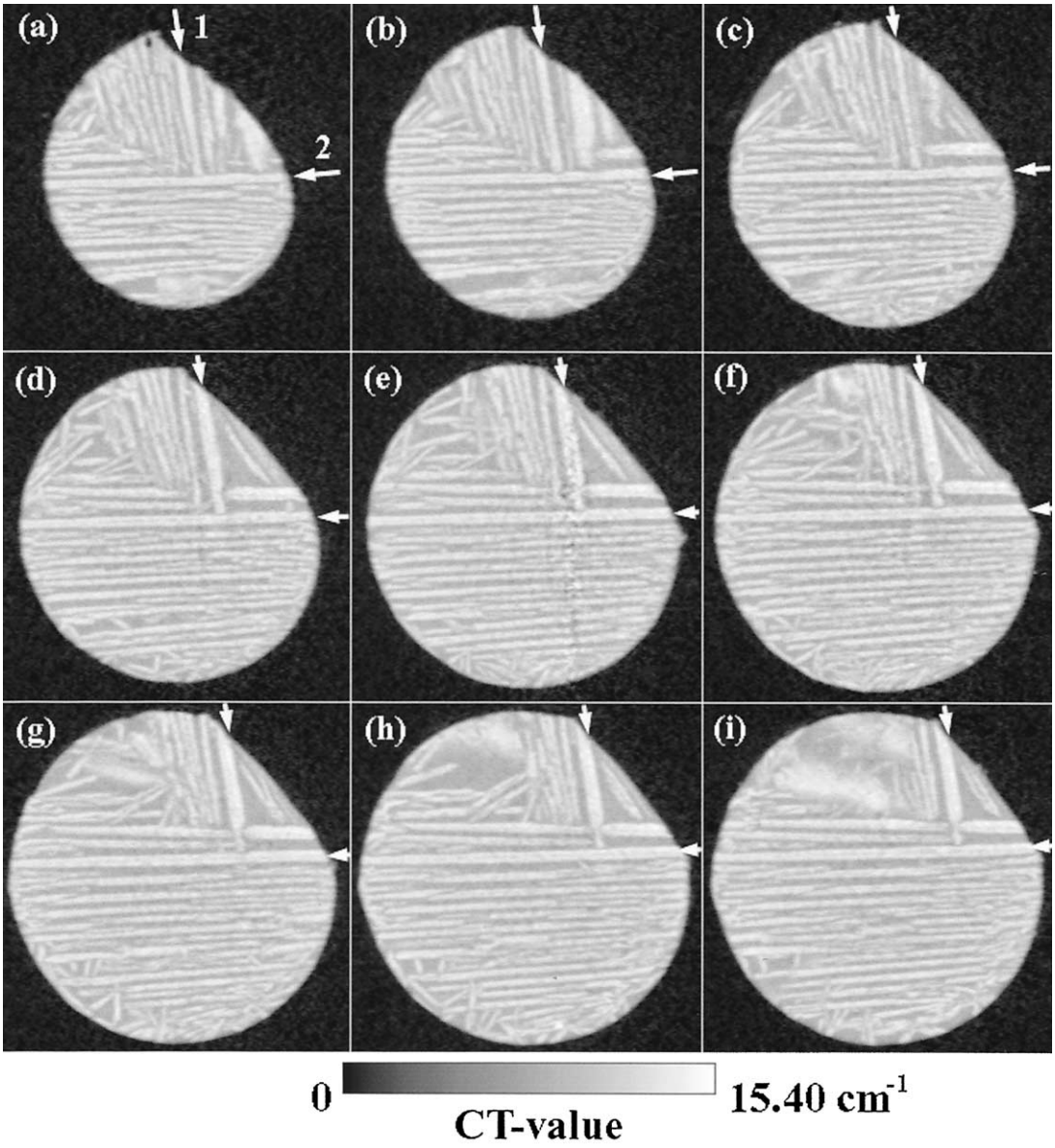

Fig. 11. X-ray CT images of run 63 (type 1 texture with type b rim heated at 1398°C for 10 min and cooled at 750°C/h (imaging No. 011026a). The width of the images is 1.410 mm. A gray scale shows the relation between CT-value and shading intensity (materials with CT values of >15.40 cm^{-1} are expressed as white pixels). Slices (a) 50 to (i) 130 are shown every 10 slices (each slice thickness is 5.83 μm and the interval of the slices is 58.3 μm). The flat surface on the upper right in each image was in contact with a graphite capsule. Arrows with two different directions show the same olivine plates, in successive slices.

skeletal and have uniform thickness. There are three possibilities for the discrepancy. One is the difference of evaporation. In natural melts, alkalis and SiO_2 should be lost by evaporation as well as FeO. This should give olivine supersaturation on the surface. This promotes nucleation and growth along the surface and a complete rim forms. The second possibility is the difference of convection. Melt composition and temperature should be homogenized except for portions very close to the surface by convection as in the experimental melts. On the other hand, convection was absent or very limited (Marangoni convection may be possible) in the micro-gravity environment for natural samples. Large compositional and temperature gradients near the surface should cause complete rim formation. The third possibility is annealing of chondrules, which will be discussed later in more detail.

The above discussion suggests that the working hypothesis for the rim formation by evaporation from chondrule melts is basically correct. A limited number of olivine rims formed in the previous experiments without apparent evaporation (Connolly et al., 1988; Lofgren and Lanier, 1990; Radomsky and Hewins, 1990). However, rim formation in the previous experiments is rare and any conditions for the rim formation are not clear.

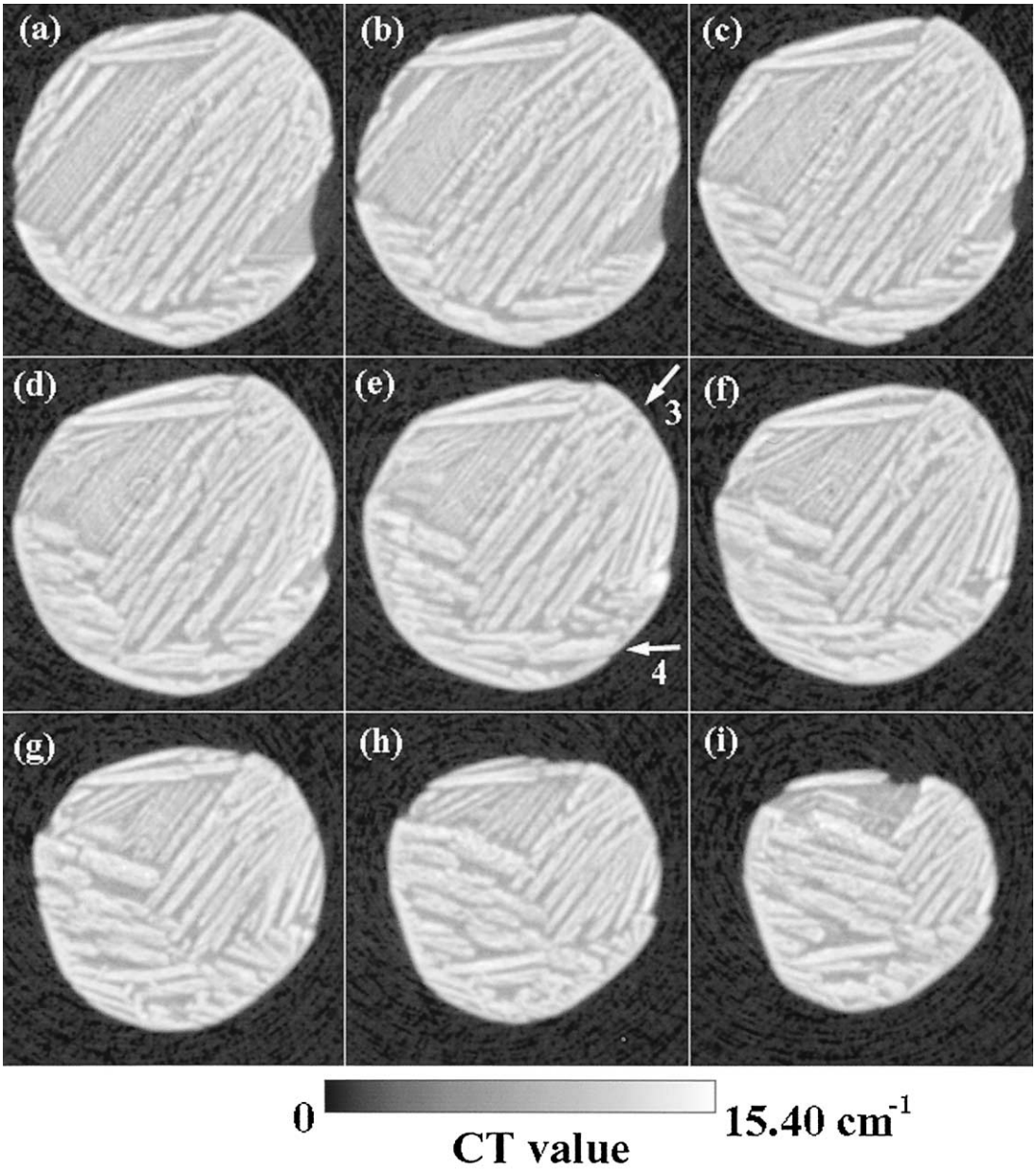

Fig. 12. X-ray CT images of run 64 (type 2 texture with type a rim heated at 1338°C for 10 min and cooled at 1000°C/h (imaging No. 011026b). The width of the images is 1.318 mm. A gray scale shows the relation between CT-value and shading intensity (materials with CT values of >15.40 cm^{-1} are expressed as white pixels). Slices (a) 100 to (i) 180 are shown every 10 slices (each slice thickness is 5.83 μm and the interval of the slices is 58.3 μm).

4.2. Classic BO Formation

The numbers of parallel olivine platelet sets can be explained by numbers of embryos for olivine nucleation as a function of ΔT_{max} and Δt_{max} as already discussed by Lofgren and Lanier (1990) and Connolly et al. (1998). In the present experiments, we obtained almost a single set of olivine platelets by using small samples (<10 mg) and succeeded in reproducing textures close to classic BO together with olivine rim by evaporation. Furthermore, the reproduction of the crystallographic orientations of olivine platelets (Fig. 14) was also confirmed for the first time in the present experiments.

The number of nucleation events in a volume of a melt spherule of diameter, r, in a unit time, N_v, is proportional to r^3. On the other hand, the number of nucleation events on the surface in a unit time, N_s, is proportional to r^2. Thus, the ratio between surface and volume nucleation (N_s/N_v) is proportional to r^{-1}. Accordingly, with decreasing r, N_s/N_v increases. This suggests that heterogeneous nucleation on the surface becomes more favorable with decreasing r. As the absolute value of N_s decreases with decreasing r as well, a single or almost single set of parallel olivine platelets forms easily as in the present experiments. The diameters of the small samples in the present

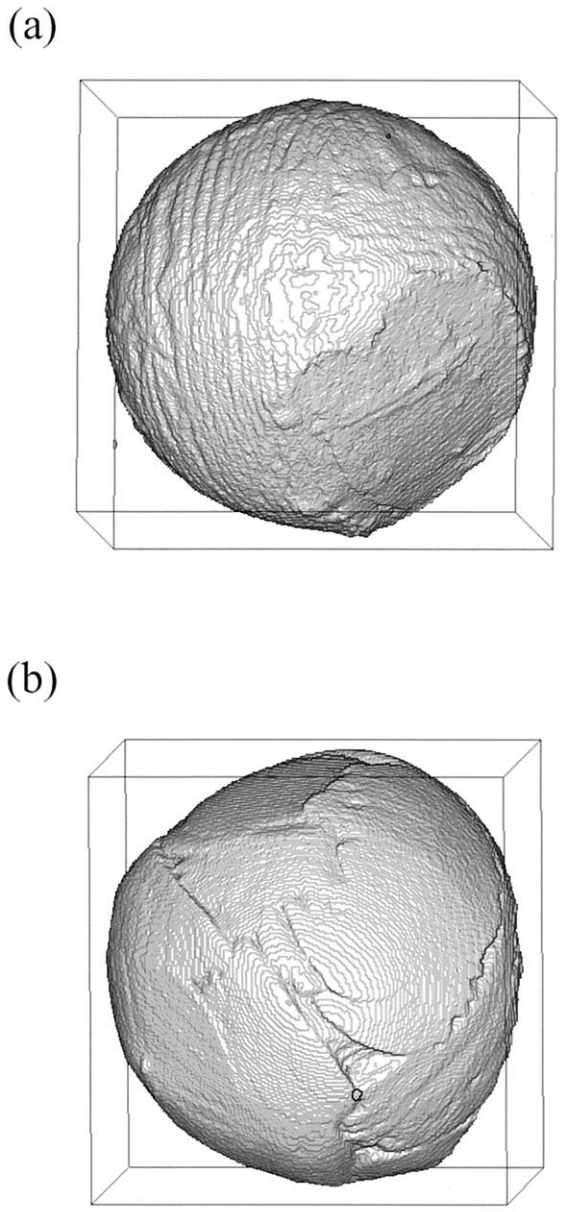

Fig. 13. Three-dimensional shapes of run products obtained by X-ray CT. (a) Run 63 (Fig. 12a: imaging No. 011026a). The flat surface on the right bottom was in contact with the graphite capsule. (b) Run 64 (Fig. 12b: imaging No. 011026b). Enlarged three-dimensional plaster models (6–6.5 cm in diameter: x ~50 magnification) were made from these data by using rapid prototyping method for more detailed observation.

study (~1.5 mm) are still larger than the mean diameters of chondrules (0.2–1.0 mm depending on the chondrite classes, e.g., Grossman et al., 1988). Therefore, perfect classic BOs were formed in the primordial nebula in contrast to the present experiments, where a definite single set of olivine plate did not form (Figs. 2f and 6). Lofgren (1996) discussed nucleation in a supercooled melt and proposed that classic BO chondrules were formed by seeding of a single particle. However, he did not consider nucleation on the surface as discussed above. Moreover, growth along the surface after nucleation is not

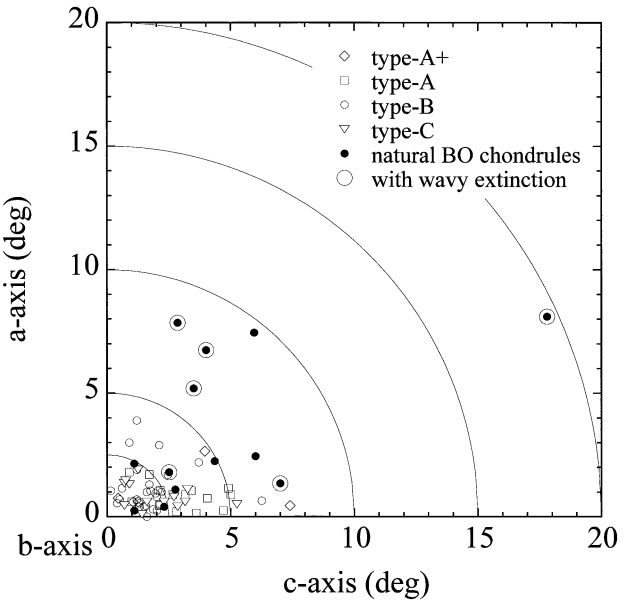

Fig. 14. A stereogram showing the directions normal to the plates of BOs (the original diagram is converted to rectangular coordinates for convenience of plotting). The directions of the a-, b- and c- axes are located to the north, zenith and east directions, respectively. Experimental charges and natural samples are shown as open and solid symbols, respectively. Natural olivine crystals with wavy extinction are also shown as enclosing circles. Because of the symmetry of olivine crystal (point group: *mmm*), all the plate directions are plotted onto an octant of the stereogram.

self-evident in his model. A single BO texture produced by a seeded experiment (fig. 15b of Radomsky and Hewins, 1990) has no rim.

Lofgren and Lanier (1990) found that the width of each olivine platelet has an inverse correlation with cooling rate. This result was explained by the degree of undercooling at the time of nucleation, ΔT_{nucl}, which was affected by the cooling

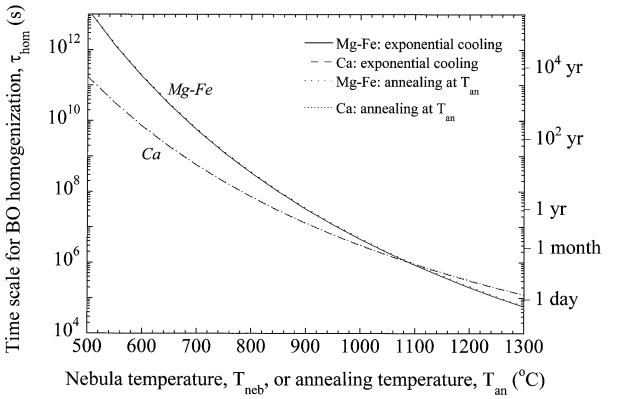

Fig. 15. A plot of timescale for BO homogenization by Mg-Fe and Ca diffusions (τ_{hom}) versus temperature of the primordial solar nebula (T_{neb}) for exponential cooling (T_0 = 1500°C and τ = 1.83 h) or annealing temperature (T_{an}) for annealing at the constant temperature. τ_{hom} is obtained by the time corresponding to the diffusion distance of the half width of the mean BO bars (10 μm) for Fa_{80} olivine at oxygen fugacity of a half log unit below the IW buffer curve.

Table 3. Estimated diffusion distances, X, of Mg-Fe and Ca in olivine in the present experiments.

Olivine composition	Fa85	Fa80	Fa85	Fa90	Fa85	
T_0 (°C)[a]	1215	1215	1215	1215	1215	1215
T_q (°C)[b]	800	800	800	800	800	800
Δ[log $f(O_2)$ (bar)][c]	IW 0	IW 2	IW 2	IW 2	IW 4	
Cooling rate (°C/h)	X(Mg-Fe)(μm)	X(Mg-Fe)(μm)	X(Mg-Fe) (μm)	X(Mg-Fe) (μm)	X(Mg-Fe) (μm)	X(Ca) (μm)
500	2.44	3.23	3.58	3.96	5.25	0.49
750	1.99	2.64	2.92	3.23	4.29	0.40
1000	1.72	2.29	2.53	2.80	3.72	0.35
1200	1.57	2.09	2.31	2.56	3.39	0.32

[a] Initial temperature.
[b] Quench temperature.
[c] Difference from the oxygen fugacity of the iron-wustite buffer curve in a log unit (e.g., IW 2: two log units above the buffer curve).

rate. Similar results were obtained in the present experiments (Fig. 4). In the present study, textures produced at the cooling rate of 1000°C/h mostly resemble to natural BO textures. The olivine platelets become more dendritic or hopper-shaped at lower cooling rates (Fig. 4a) while they become finer and resemble to radial olivine texture at higher cooling rates (Fig. 2a). The cooling rate to produce BO textures for the FeO-rich melt composition is consistent with that of previous studies having FeO-poor compositions (Tsuchiyama and Nagahara, 1981; Hewins, 1988; Lofgren and Lanier, 1990; Radomsky and Hewins, 1990). However, olivine platelets in the present and previous experiments are always dendritic or hopper-shaped and not closely similar to those in the most natural BO chondrules. In addition, Mg-Fe and Ca zonations of olivine platelets, which were also reported in Lofgren and Lanier (1990), are not consistent with natural BO chondrules. Heterogeneous zoning is present even in the charges with the lowest cooling rates (500°C/h) in the present experiments while natural BOs in unequilibrated chondrites show homogenized Mg-Fe zoning (Miyamoto et al., 1986; Weisberg, 1987).

The decrease of olivine platelet width with increasing t_{max} (Fig. 6) can also be explained by ΔT_{nucl} if we consider the survival of olivine embryos at the peak temperature. ΔT_{nucl} should increase and thus the width decreases with increasing t_{max}. Therefore, typical BO textures including rim formation require high heating temperatures (~100–200°C above the liquidus) and short heating durations (~10 s). This prefers the flash melting model for chondrule formation (e.g., Connolly and Hewins, 1998).

4.3. Annealing of BO

As mentioned above, we reproduced the basic features of BO: (i) olivine rim, (ii) single or multiple set(s) of parallel olivine platelets and (iii) crystallographic orientation of olivine. However, we cannot reproduce some features: (iv) width and precise morphology of olivine rims, (v) precise morphology of olivine platelets and (vi) lack of compositional zoning.

The discrepancy of the olivine rim width can be explained by evaporation of components other than FeO (e.g., Na_2O and SiO_2) and/or crystallization under convection-free (or convection-less) conditions as already discussed. One or both processes might contribute to rim development in natural BO. However, the other discrepancies cannot be explained by the above processes. All the discrepancies might be explained by annealing after chondrule formation.

Discrepancies of (iv) and (v) could be explained by decrease of the surface area of olivine crystals during annealing. This is a kind of Ostwald ripening (or grain coarsening) to reduce the interfacial energies between olivine and melt (or glass). Thin and dendritic (sometimes polycrystalline?) olivine rims should become thick and platy (single) crystals. At the same time, dendritic or hopper-shaped olivine platelets should become simply platy morphologies. Hewins and Fox (a personal communication) reheated BO spherules at a temperature below the liquidus but the bars were still rather skeletal. However, no systematic experiments have been done and we do not have any quantitative kinetic data on such ripening process at present. Therefore, we cannot discuss this process in more detail further.

Discrepancy of (vi) could also be explained by annealing. This process can be discussed quantitatively using diffusion of elements in olivine. Miyamoto et al. (1986) discussed zoning of olivine crystals in chondrules of unequilibrated ordinary chondrites. They calculated Mg-Fe and Ca zoning profiles during cooling numerically using the diffusion equation with the initial conditions of zoning profiles of olivine in type 3 chondrites as a function of initial temperature and linear cooling rate. In the present study, the homogenization process is discussed using diffusion distance, X, for simplicity (see Appendix for detail). The Mg-Fe interdiffusion coefficient in olivine of Miyamoto and Mikouchi (1998) and Miyamoto et al. (2002), which was modified from Misener (1974) by considering variation with oxygen fugacity similar to that of Buening and Buseck (1973), was adopted here because this gives the best fit to experimentally produced diffusion profiles. The Ca diffusion coefficient in olivine of Jurewicz and Watson (1988), which gives the best fit to experimentally produced diffusion profiles (Miyamoto and Mikouchi, 1998), was adopted too.

Diffusion distances for the present experimental conditions (initial temperature: T_0 = 1215°C, quench temperature: T_q = 800°C, cooling rate: θ = 500–1200°C/h, olivine composition = Fa_{80}-Fa_{90}) were calculated by Eqn. 5 in Appendix (Table 3). Those of Mg-Fe are 2–5 μm at the oxygen fugacity, $f(O_2)$, of 2–4 log unit above the IW buffer curve, which was estimated

Table 4. Estimated diffusion distances, X, of Mg-Fe and Ca in olivine in the experiments of Lofgren and Lanier (1990).

Olivine composition	Fa10	Fa15	Fa20	Fa25	Fa30	
T_0 (°C)[a]	1590	1590	1590	1590	1590	1590
T_q (°C)[b]	1200	1200	1200	1200	1200	1200
Δ[log $f(O_2)$ (bar)][c]	IW-0.5	IW-0.5	IW-0.5	IW-0.5	IW-0.5	
Cooling rate (°C/h)	X(Mg-Fe) (μm)	X(Mg-Fe) (μm)	X(Mg-Fe) (μm)	X(Mg-Fe) (μm)	X(Mg-Fe) (μm)	X(Ca) (μm)
100	8.50	9.54	10.66	11.86	13.15	5.73
500	3.80	4.27	4.77	5.30	5.88	2.56
1000	2.69	3.02	3.37	3.75	4.16	1.81
1500	2.19	2.46	2.75	3.06	3.40	1.48
2300	1.77	1.99	2.22	2.47	2.74	1.19

[a] Initial temperature.
[b] Quench temperature.
[c] Difference from the oxygen fugacity of the iron-wustite buffer curve in a log unit (e.g., IW 2: two log units above the buffer curve).

from the residual oxygen in vacuum as already mentioned (note that Mg-Fe diffusion coefficient has a week $f(O_2)$-dependence: $D_{Mg\text{-}Fe} \propto f(O_2)^{1/6}$) and those of Ca are 0.3–0.5 μm. As T_0 was adopted as the liquidus temperature but olivine started to grow at some undercoolings, the above values are the upper limits. These diffusion distances are less than the typical width of olivine bars (10–100 μm) and thus Mg-Fe and Ca zonings formed by the growth of olivine should not be erased by the cooling. This is consistent with the observation (Figs. 5 and 10). Diffusion distances for the experimental conditions of Lofgren and Lanier (1990) were also calculated (Table 4: T_0 = 1590°C, T_q = 1200°C, θ = 100–2300°C/h, olivine composition = Fa_{10}-Fa_{30}, $f(O_2)$ = a half log unit below the IW buffer curve). They are 2–6 μm for Mg-Fe and 1–3 μm for Ca at θ = 500–2300°C/h, where BO textures were formed. This is also consistent with observed zonings of Mg-Fe and Ca.

Table 5 shows diffusion distances for natural chondrules estimated by exponential cooling process of Eqn. 6 in Appendix. Cooling rates corresponding to each cooling time, τ, at two different T_0 (1600 and 1500°C) are shown. Olivine compositions of Fa_{10}-Fa_{30} are considered because the composition ranges of BO are Fa_5-Fa_{40} for L3, Fa_5-Fa_{30} for LL3, and Fa_5-Fa_{20} for H3, respectively (the mean Fa content is 17.5 for H3 and LL3 and 23.3 for L3) (Weisberg, 1987). $f(O_2)$ of a half log unit below the IW buffer curve (Lofgren and Lanier, 1990) is reasonable for chondrule formation although intrinsic oxygen fugacities of ordinary chondrites of Brett and Sato (1984) (~3 log units below the IW buffer curve) were used by Miyamoto et al. (1986). If T_{neb} is sufficiently low (e.g., <300°C) and the cooling rate at T_0 is 500–2000°C/h (τ = 1–3 h) appropriate for BO texture formation, X = 1–6 μm and 1–3 μm for Mg-Fe and Ca diffusions, respectively. As the mean width of olivine bars is ~20 μm (Miyamoto et al., 1986) growth zoning of Mg-Fe and Ca in BO is expected to remain in a simple cooling. However, this is not consistent with observation that Mg-Fe zoning was not found in BO in the type 3 ordinary chondrites (Miyamoto et al., 1986; Weisberg, 1987). On the other hand, slight zoning of Ca was found by Miyamoto et al. (1986) while Weisberg (1987) did not find Ca zoning.

To discuss homogenization in BO by annealing, diffusion distances during exponential cooling to different temperatures of the primordial solar nebula (T_{neb} = 500–1300°C) were calculated (Fa_{20} olivine, T_0 = 1500°C, the cooling rate at T_0 is 1000°C/h (τ = 1.83 h) and the oxygen fugacity of a half log unit below the IW buffer curve). Time required for the diffusion distance of 10 μm (the mean half width of olivine bars) can be regarded as the timescale for BO homogenization, τ_{hom}. This is plotted against T_{neb} for Mg-Fe and Ca diffusions in Figure 15. The timescale at constant annealing temperature (T_{an}) is also shown in Figure 15 ($\tau_{hom} = X^2/D(T_{an})$ at X = 10 μm). The above two kinds of τ_{hom} are almost the same because τ_{hom} is sufficiently larger than the cooling timescale, τ. As the activation energy of the Ca diffusion is larger than that of the Mg-Fe diffusion, cross over of τ_{neb} for Mg-Fe and Ca diffusions occurs at ~1100°C. Homogeneous Mg-Fe and slightly Ca zonings (Miyamoto et al., 1986) cannot be explained by thermal metamorphism because Ca zoning should be homogenized before Mg-Fe zoning at typical metamorphic temperatures well below 1100°C. The observation can be explained by annealing at relatively high temperatures for short duration (e.g., 1200°C for a few days). In this case chondrules should cool to these moderately high temperature, stay there for a few days to a month and cool again to lower temperature. More likely, repeated heating of chondrules to subliquidus temperatures, which should correspond to recycling process of chondrules (e.g., Jones, 1996a,b; Jones and Danielson, 1997), seems to be responsible for the observed zoning. Glass in BO chondrules may crystallize during annealing. However, if diffusion distance in a glass (or melt) is long at high temperatures, olivine overgrowth should occur together with Ostwald ripening rather than new nucleation events in the glass. The diffusion distances of 1–6 μm and 1–3 μm for Mg-Fe and Ca diffusions, respectively, in a single cooling event as mentioned above, may correspond to reheating by 5–10 times.

Another possible process for the Mg-Fe homogenization is FeO-metasomatism, which might occur in the primordial solar nebula or in a parental body (Krot et al., 1995). Most of the Mg-Fe compositions of BO might be homogenized by this process. In this case, presence or absence of Ca zoning (Miyamoto et al., 1986; Weisberg, 1987) alone should be discussed in Figure 15. If thermal metamorphism was responsible for the Ca homogenization, heating of the order of 10^4 yr was required for the slight zoning at 500°C. However, textural modification of olivine rims and plates may not be explained at such low

Table 5. Estimated diffusion distances, X, of Mg-Fe and Ca in olivine during chondrule formation.

	Olivine composition	Fa10	Fa20	Fa30	Fa10	Fa20	Fa30	
	T_0 (°C)[a]	1600	1600	1600	1600	1600	1600	1600
	T_{neb} (°C)[b]	300	300	300	300	300	300	300
	Δ[log $f(O_2)$ (bar)][c]	IW-0.5	IW-0.5	IW-0.5	IW-3	IW-3	IW-3	
τ (h)[d]	Cooling rate (°C/h) at 1600°C	X(Mg-Fe) (μm)	X(Mg-Fe) (μm)	X(Mg-Fe) (μm)	X(Mg-Fe) (μm)	X(Mg-Fe) (μm)	X(Mg-Fe) (μm)	X(Ca) (μm)
0.3	6243.3	1.17	1.46	1.80	0.72	0.90	1.12	0.79
1	1873.0	2.13	2.67	3.29	1.32	1.65	2.04	1.44
3	624.3	3.69	4.62	5.70	2.28	2.86	3.53	2.50
10	187.3	6.73	8.44	10.41	4.16	5.22	6.44	4.57
30	62.4	11.65	14.61	18.03	7.21	9.04	11.16	7.91
100	18.7	21.28	26.68	32.93	13.17	16.51	20.38	14.44
	Olivine composition	Fa10	Fa20	Fa30	Fa10	Fa20	Fa30	
	T_0 (°C)[a]	1500	1500	1500	1500	1500	1500	1500
	T_{neb} (°C)[b]	300	300	300	300	300	300	300
	Δ[log $f(O_2)$ (bar)][c]	IW-0.5	IW-0.5	IW-0.5	IW-3	IW-3	IW-3	
τ (h)[d]	Cooling rate (°C/h) at 1500°C	X(Mg-Fe) (μm)	X(Mg-Fe) (μm)	X(Mg-Fe) (μm)	X(Mg-Fe) (μm)	X(Mg-Fe) (μm)	X(Mg-Fe) (μm)	X(Ca) (μm)
0.3	5910.0	0.73	0.92	1.14	0.45	0.57	0.70	0.56
1	1773.0	1.32	1.67	2.08	0.82	1.03	1.29	1.02
3	591.0	2.29	2.90	3.60	1.42	1.79	2.23	1.76
10	177.3	4.19	5.29	6.57	2.59	3.27	4.07	3.22
30	59.1	7.25	9.16	11.38	4.49	5.67	7.04	5.58
100	17.7	13.24	16.72	20.77	8.20	10.35	12.86	10.18

[a] Initial temperature.
[b] Temperature of the solar nebula (final temperature).
[c] Difference from the oxygen fugacity of the iron-wustite buffer curve in a log unit (e.g., IW 2: two log units above the buffer curve).
[d] Cooling time scale.

temperatures. Therefore, it is likely that BO textures and their compositions were modified by repeated heating, which corresponds to chondrule recycling process. The presence or absence of Ca zoning can be explained by the number and intensity of the repeated heating. It was also reported that Mg-Fe zoning is present in one BO and absent in another BO in the most unequilibrated chondrite (Semarkona, LL3.0) (private communication of John DeHart cited in Lofgren and Lanier, 1990). This may be also explained by the repeated heating. Zoning and scarcity of glass inclusions and dendritic side arms of BOs in the most unequilibrated chondrite should be examined in more detail to elucidate the annealing processes. The present discussion about the annealing temperature is largely dependent on the values of the diffusion coefficients of Mg-Fe and Ca. Systematic experiments are also required to elucidate homogenization and grain growth of BOs.

4.4. Open System Behavior of Chondrule Formation

Whether or not chondrules formed as open systems has been debated for a long time (Sears et al., 1996). Chemical variety of chondrules was basically established by evaporation-loss of relatively volatile elements (e.g., alkalis, Fe and Si) and/or chemical reaction with evaporated species during chondrule formation as open systems (e.g., Alexander, 1996; Huang et al., 1996; Sears et al., 1996) or was inherited entirely from the variation of chondrule precursors as closed systems (e.g., Grossman, 1988; Rubin and Wasson, 1988). Recent experimental and theoretical studies proposed that open system behavior was important during chondrule formation (Hewins, 1997; Tsuchiyama and Tachibana, 1999; Alexander et al., 2000; Cohen et al., 2000; Galy et al., 2000; Ozawa and Nagahara, 2001). The present results on the formation of BO rim suggest that chondrules were formed as open systems, where evaporation of elements occurred during heating and subsequent cooling. Formation of porphyritic textures was explained by open system behavior of chondrule formation (Cohen et al., 2000). In this study, open system behavior also explains formation of another type of chondrule texture (cooled from perfectly molten state), that is BO texture.

Evaporation during heating in the chondrule formation might cause isotopic mass fractionation by Rayleigh fractionation (e.g., Esat et al., 1986; Davis et al., 1990; Wang et al., 2001). However, such mass fractionation has not been observed in chondrules (e.g., Grossman et al., 1998; Alexander et al., 2000). The lack of isotopic mass fractionation has been explained by recondensation of evaporated materials, or isotopic equilibration between chondrules and surrounding gas (Tsuchiyama et al., 1999; Alexander et al., 2000; Ozawa and Nagahara, 2001). Thus, chondrules were formed as an open system and their textures and chemical compositions were affected by

evaporation while the isotopic compositions were largely affected by isotopic reequilibration.

Acknowledgments—This work was financially supported in part by Grant-in-Aid for Scientific Research (A) (11304035) from the Japan Society for the Promotion of Science. The CT experiments were made by the research project of 2000A0124-COM-np at SPring-8. We are grateful to Mr. M. Yagai and Ms. M. Komuro of TACC/AIST for making the enlarged three-dimensional plaster models and Drs. R. H. Hewins and H. C. Connolly Jr. for critical reviews.

Associate editor: C. Koeberl

REFERENCES

Alexander C. M. O'D. (1996) Recycling and volatile loss in chondrule formation. In *Chondrules and the Protoplanetary Disk* (eds. R. H. Hewins, R. H. Jones, and E. R. D. Scott), pp. 233–241. Cambridge University Press.

Alexander C. M. O'D., Grossmann J. N., Wang J., Zanda B., Bourot-Denise M., and Hewins R. H. (2000) The lack of potassium-isotopic fractionation in Bishunpur chondrules. *Meteoritics Planet. Sci.* **35,** 859–868.

Blander M., Planner H. N., Keil K., Nelson L. S., and Richardson N. L. (1976) The origin of chondrules: Experimental investigation of metastable liquid in the system Mg_2SiO_4-SiO_2. *Geochim. Cosmochim. Acta* **40,** 889–896.

Bowen N. L. and Schairer J. F. (1935) The system MgO-FeO-SiO_2. *Am. J. Sci. Ser. 5* **29,** 151–217.

Brett R. and Sato M. (1984) Intrinsic oxygen fugacity measurements on seven chondrites, a pallasite, and a tektite and the redox state of meteorite parent bodies. *Geochim. Cosmochim. Acta* **48,** 111–120.

Buening D. K. and Buseck P. R. (1973) Fe-Mg lattice diffusion in olivine. *J. Geophys. Res.* **78,** 6852–6862.

Cohen B. A. (2002) Chondrule formation by open-system melting of nebular condensates. Ph.D. thesis. Rutgers University.

Cohen B. A., Hewins R. H., and Yu Y. (2000) Evaporation in the young solar nebula as the origin of the "just-right" melting of chondrules. *Nature* **406,** 600–602.

Connolly H. C. Jr., Radomsky P. M., and Hewins R. H. (1988) Chondrule texture: The influence of bulk composition and heating time for uniform thermal conditions. *Lunar Planet. Sci.* **19,** 205–206.

Connolly H. C. Jr. and Hewins R. H. (1991) The influence of bulk composition and dynamic melting conditions on olivine chondrule textures. *Geochim. Cosmochim. Acta* **55,** 2943–2950.

Connolly H. C. Jr. and Hewins R. H. (1995) Chondrules as products of dust collisions with totally molten droplets within a dust-rich nebular environment: An experimental investigation. *Geochim. Cosmochim. Acta* **59,** 3231–3246.

Connolly H. C. Jr., Jones B. D., and Hewins R. H. (1998) The flash melting of chondrules: An experimental investigation into the melting history and physical nature of chondrule precursors. *Geochim. Cosmochim. Acta* **62,** 2725–2735.

Davis A. M., Hashimoto A., Clayton R. N., and Mayeda T. K. (1990) Isotope mass fractionation during evaporation of Mg_2SiO_4. *Nature* **347,** 655–658.

Donaldson C. H. (1976) Experimental investigation of olivine morphology. *Contrib. Mineral. Petrol.* **57,** 187–213.

Esat T. M., Spear R. H., and Taylor S. R. (1986) Isotope anomalies induced in laboratory distillation. *Nature* **319,** 576–578.

Galy A., Young E. D., Ash R. D., and O'Nions R. K. (2000) The formation of chondrules at high gas pressures in the solar nebula. *Science* **290,** 1751–1754.

Grossman J. N., Rubin A. E., Nagahara H., and King E. A. (1988) Properties of chondrules. In *Meteoritics and the Early Solar System* (eds. J. F. Kerridge and M. S. Matthews), pp. 619–659. University of Arizona Press.

Hewins R. H. (1988) Experimental studies of chondrules. In *Meteoritics and the Early Solar System* (eds. J. F. Kerridge and M. S. Matthews), pp. 660–679. University of Arizona Press.

Hewins R. H., Yu Y., Zanda B., and Bourot-Denise M. (1997) Do nebular fractionations, evaporative losses, or both, influence chondrule compositions? *Antarct. Meteorites Res.* **10,** 275–298.

Hofmann A. W. (1980) Diffusion in natural silicate melts: A critical review. In *Physics of Magmatic Processes* (ed. R. B. Hargraves), pp. 385–417. Princeton University Press.

Huang S., Lu J., Prinz M., Weisberg M. K., Benoit P. H., and Sears D. W. G. (1996) Chondrules: Their diversity and the role of open-system processes during their formation. *Icarus* **122,** 316–346.

Jones R. H. (1996a) FeO-rich, porphyritic pyroxene chondrules in unequilibrated ordinary chondrites. *Geochim. Cosmochim. Acta* **60,** 3115–3138.

Jones R. H. (1996b) Relict grains in chondrules: Evidence for chondrule recycling. In *Chondrules and the Protoplanetary Disk* (eds. R. H. Hewins, R. H. Jones, and E. R. D. Scott), pp. 163–172. Cambridge University Press.

Jones R. H. and Danielson L. R. (1997) A chondrule origin for dusty relict olivine in unequilibrated chondrules. *Meteoritics Planet. Sci.* **32,** 753–760.

Jurewicz A. J. G. and Watson E. B. (1988) Cations in olivine, Part 2: Diffusion in olivine xenocrysts, with applications to petrology and mineral physics. *Contrib. Mineral Petrol.* **99,** 186–201.

Krot A. N., Scott E. R. D., and Zolensky M. E. (1995) Mineralogical and chemical modification of components in CV3 chondrites – nebular or asteroidal processing. *Meteoritics* **30,** 748–775.

Lofgren G. E. (1987) Dynamic crystallization experiments on chondrule melts of porphyritic olivine composition: Effect of annealing at 1200 and 1000°C on major and minor element zoning and concentration. *Lunar Planet. Sci.* **18,** 566–567.

Lofgren G. E. (1989) Dynamic crystallization experiments on chondrule melts of porphyritic olivine composition: Textures experimental and natural. *Geochim. Cosmochim. Acta* **53,** 461–470.

Lofgren G. E. (1996) A dynamic crystallization model for chondrule melts. In *Chondrules and the Protoplanetary Disk* (eds. R. H. Hewins, R. H. Jones, and E. R. D. Scott), pp. 187–196. Cambridge University Press.

Lofgren G. E. and Russell W. J. (1985) Dynamic crystallization experiments on chondrule melts of porphyritic olivine composition. *Lunar Planet. Sci.* **16,** 499–500.

Lofgren G. E. and Lanier A. B. (1990) Dynamic crystallization study of barred olivine chondrules. *Geochim. Cosmochim. Acta* **54,** 3537–3551.

McCullough E. C. (1975) Photon attenuation in computed tomography. *Med. Phys.* **2,** 307–320.

Misener D. J. (1974) Cationic diffusion in olivine to 1400°C and 35 kbar. *Publ. Carnegie Inst. Wash.* **634,** 117–129.

Miyamoto M., McKay D. S., McKay G. A., and Duke M. B. (1986) Chemical zoning and homogenization of olivines in ordinary chondrites and implications for thermal histories of chondrules. *J. Geophys. Res.* **91,** 12803–12816.

Miyamoto M. and Mikouchi T. (1998) Evaluation of diffusion coefficients of Fe-Mg and Ca in olivine. *Mineral. J.* **20,** 9–18.

Miyamoto M., Mikouchi T., and Arai T. (2002) Comparison of Fe-. Mg interdiffusion coefficients in olivine. *Antarct. Meteorite Res.* **15,** 143–151.

Nelson L. S., Blander M., Skaggs S. R., and Keil K. (1972) Use of CO_2 laser to prepare chondrule-like spherules from supercooled molten oxide and silicate droplets. *Earth Planet. Sci. Lett.* **14,** 338–344.

Noguchi T. (2002) Estimation of three-dimensional internal structures of some barred olivine chondrules in Allende (CV3) chondrite. *Antatct. Meteorite Res.* **15,** 59–77.

Ozawa K. and Nagahara H. (2001) Chemical and isotopic fractionations by evaporation and their cosmochemical implications. *Geochim. Cosmochim. Acta* **65,** 2171–2199.

Radomsky P. M. (1988) Dynamic crystallization experiments on magnesian olivine-rich and pyroxene-rich chondrule composition. M. S. thesis, Rutgers University.

Radomsky P. M. and Hewins R. H. (1987) Dynamic crystallization experiments on an average type-I (MgO-rich) chondrule composition. *Lunar Planet. Sci.* **18,** 808–809.

Radomsky P. M. and Hewins R. H. (1990) Formation condition of pyroxene-olivine and magnesian olivine chondrules. *Geochim. Cosmochim. Acta* **54,** 3475–3490.

Rubin A. E. and Wasson J. T. (1988) Chondrules and matrix in the Ornans CO3 meteorite: Possible precursor components. *Geochim. Cosmochim. Acta* **52,** 425–432.

Sears D. W. G., Huang S., and Benoit P. (1996) Open-system behavior during chondrule formation. In *Chondrules and the Protoplanetary Disk* (eds. R. H. Hewins, R. H. Jones, and E. R. D. Scott), pp. 221–231. Cambridge University Press.

Tsuchiyama A., Nagahara H., and Kushiro I. (1980) Experimental reproduction of textures of chondrules. *Earth Planet. Sci. Lett.* **48,** 155–165.

Tsuchiyama A. and Nagahara H. (1981) Effect of precooling thermal history and cooling rate on the texture of chondrules: A preliminary report. *Mem. Natl. Inst. Polar Res.* **20,** 175–192.

Tsuchiyama A. and Fujimoto S. (1995) Evaporation experiments on metallic iron in vacuum. *Proc. NIPR Symp. Antarct. Meteorites* **8,** 205–213.

Tsuchiyama A. and Tachibana S. (1999) Evaporation rates of elements, such as sodium, from melts under solar nebula conditions. *Lunar Planet. Sci.* **30,** 1535.

Tsuchiyama A., Tachibana S., and Takahashi T. (1999) Evaporation of forsterite in the primordial solar nebula; rates and accompanied isotopic fractionation. *Geochim. Cosmochim. Acta* **63,** 2451–2466.

Tsuchiyama A., Kawabata T., Kondo M., Uesugi K., Nakano T., Suzuki Y., Yagi N., Umetani K., and Shirono S. (2000) Spinning chondrules deduced from their three-dimensional structures by X-ray CT method. *Lunar Planet. Sci.* **31,** 1566.

Tsukamoto K., Satoh H., Takamura Y., and Kuribayashi K. (1999) A new approach for the formation of olivine-chondrules by aero-acoustic levitation. *Antarct. Meteorites* **24,** 179–181.

Tsukamoto K., Kobatake H., Nagashima K., Satoh H., and Yurimoto H. (2001) Crystallization of cosmic materials in microgravity. *Lunar Planet. Sci.* **32,** 1846.

Uesugi K., Tsuchiyama A., Nakano T., Suzuki Y., Yagi N., Umetani K., and Kohmura Y. (1999) Development of micro-tomography imaging system for rocks and mineral samples. In *Developments in X-ray Tomography 2* (ed. U. Bonse), pp. 214–221. Proc. SPIE 3772.

Wang J., Davis A. M., Clayton R. N., Mayeda T. K., and Hashimoto A. (2001) Chemical and isotopic fractionation during the evaporation of the FeO-MgO-SiO_2-CaO-Al_2O_3-TiO_2 rare earth element melt system. *Geochim. Cosmochim. Acta* **65,** 479–494.

Weisberg M. K. (1987) Barred olivine chondrules in ordinary chondrites. *J. Geophys. Res.* **92,** E663–E678.

APPENDIX

Estimation of Diffusion Distance during Cooling

Diffusion distance, X, during cooling is estimated from the following equation:

$$X^2 = \int_0^t D dt, \tag{1}$$

where t is time and diffusion coefficeint, D, has an Arrhenius relation:

$$D = D_0 e^{-E/RT}, \tag{2}$$

where D_0 is preexponential term, E is activation energy, R is the gas constant, and T is temperature. Two kinds of cooling processes are assumed. One is linear cooling:

$$T = T_0 - \theta t \tag{3}$$

and the other is exponential cooling:

$$T = (T_0 - T_{neb})\, e^{-t/\tau} + T_{neb}, \tag{4}$$

where T_0 is the initial temperature at $t = 0$, T_{neb} is the temperature of the primordial solar nebula, θ is cooling rate, and τ is cooling timescale ($\theta = T/\tau$ at a given T). Eqns. 1–4 give the diffusion distance as a function of T as follows. For linear cooling,

$$X^2 = \frac{D_0 E}{R\theta}\left[\left(-\frac{e^{-z}}{z} + \frac{e^{-z_0}}{z_0}\right) + \{-Ei\,(-z) + Ei(-z_0)\}\right], \tag{5}$$

where $z \equiv E/RT$ and Ei is the integral exponential function,

$$\left(Ei\,(-z) = -\int_z^\infty \frac{e^{-z}}{z}\right).$$

If T is sufficiently small ($z \gg 1$),

$$X^2 \approx D\,(T_0)\,\frac{RT_0^{\,2}}{E\theta}. \tag{5'}$$

For exponential cooling, the integration was calculated nemerically. If $T_{neb} \sim 0$,

$$X^2 = D_0\tau\,[-Ei(-z_0) + Ei(-z)] \tag{6}$$

and if T is sufficiently small ($z \gg 1$),

$$X^2 \approx D\,(T_0)\,\frac{RT_0}{E}\,\tau. \tag{6'}$$

In the case of $T < 1000$ K, $z > 20$ ($E \sim 150$–200 kJ/mol [Hofmann, 1980] and $R \sim 8$ J/mol K), and thus Eqns. 5′ and 6′ approximately hold.